MŰEGYETEM 1782

Diploma thesis

Electron Spin Resonance Spectroscopy on Graphite Intercalation Compounds

Gábor Fábián

Thesis advisor: Dr. Ferenc Simon
associate professor
Department of Physics
Institute of Physics
BME

Budapest University of Technology and Economics
BME

2011

Diplomatéma-kiírás

Témavezető:

Neve:	Simon Ferenc
Tanszéke:	Fizika Tanszék
E-mail címe:	simon@esr.phy.bme.hu
Telefonszáma:	463-3816

Azonosító: DM-2010-81

Diplomatéma címe: Elektron spin rezonancia spektroszkópia szén nanocsöveken

Melyik szakiránynak ajánlott? *"Kutatófizikus"*

A jelentkezővel szemben támasztott elvárások: Jeles eredményű BSc a fizikus szakirányon.

Leírása: Az elmúlt évtized a nanoszerkezetű anyagok és azon belül is az ún. szén nanocsövek kutatásának rohamos fejlődését hozta. A szén nanocsövek a szén negyedik módosulatát képviselik a grafit, gyémánt és fullerének után. A terület megoldandó technológiai problémái mellett számos alapvető kérdés, mint pl. a szén nanocsövek alapállapota és Fermi felület közeli állapotsűrűsége jelenleg is intenzíven kutatott. Az MsC diplomamunka ezen kutatásokhoz járul hozzá szintézis és szilárdtestspektroszkópia alkalmazásával, e két módszer kombinálásával. A munkához fontos az elméleti ismeretekben, szilárdtestfizikában való biztos jártasság, előny a jó gyakorlati érzék, önállóság és a kísérleti munkához való affinitás.

Önállósági nyilatkozat

Alulírott Fábián Gábor, a Budapesti Műszaki és Gazdaságtudományi Egyetem Fizikus mesterszak (MSc) kutatófizikus szakirányának hallgatója kijelentem, hogy ezt a diplomamunkát meg nem engedett segítség igénybevétele nélkül, saját magam készítettem. Minden olyan szövegrészt, adatot, diagramot, ábrát, vagy bármely más elemet, melyet szó szerint vagy azonos értelemben, de átfogalmazva más forrásából vettem, egyértelműen megjelöltem a forrás megadásával.

Budapest, 2011. június 1.

Fábián Gábor

Köszönetnyilvánítás

Elsőként szüleimnek tartozom köszönettel, hogy tanulmányaim során töretlenül támogattak, és bíztak bennem.

Ezúton fejezem ki hálámat témavezetőmnek, Dr. Simon Ferencnek, aki rendkívüli lelkesedéssel vont be a kísérleti munka minden részébe, és vezetett be a kísérleti fizika világába. Segítsége és tanácsai nélkül jelen dolgozat és eddigi eredményeim nem valósulhattak volna meg. Köszönöm a dolgozat többszöri alapos átnézését, és az útmutatást a lehető legjobb diplomamunka megírásához.

Köszönöm Prof. Mihály György tanszékvezető úrnak a méréseimhez szükséges infrastruktúra biztosítását. A tanszék mágneses rezonancia csoportjának munkatársainak: Prof. Jánossy Andrásnak, Dr. Fehér Titusznak, Antal Ágnes és Karaszi Mihály doktorandusz-hallgatóknak köszönöm, hogy lehetőséget biztosítottak a nagyfrekveciás ESR spektrométer használatára, és segítettek kezelésében, illetve ha bármilyen kérdéssel is fordultam hozzájuk. A kutatásomhoz szükséges elméleti háttérért és számolásokért Dr. Dóra Balázst illeti köszönet. Szirmai Péternek köszönöm türelmét és segítségét a közös munkánkban.

Hálás vagyok Prof. Forró Lászlónak a nyári gyakorlatokért a lausanne-i EPF-en, amelyek bevezettek a tudományos kutatómunka folyamatába. Prof. Thomas Pichlernek köszönöm a 2010-es nyári szakmai gyakorlatot a Bécsi Egyetemen, melynek eredményeként megszülethetett az első saját tudományos publikációm.

Végezetül még megköszönném általános iskolai fizikatanárnőmnek, Amstadt Arankának, hogy tárgyának oktatásával rávezetett a fizika tudományának ösvényeire.

Acknowledgements

I dedicate this thesis to my parents for their ceaseless trust and encouragement on my path so far.

I am indebted to Dr. Ferenc Simon for getting my scientific career started by keeping a good balance of firm guidance and creative freedom, allowing me to reach my potential, and produce results already. I thank him for his help and advice in the writing of this thesis.

I acknowledge Prof. György Mihály for the scientfic enviroment at the Department of Physics which he has fostered as the head of the department.

I am grateful to Prof. László Forró for the summer internships at the EPFL, which have significantly broadened my scope of experimental solid state physics methods. I thank Prof. Thomas Pichler for the 2010 summer internship at the University of Vienna, which resulted in my premier first author publication.

Abstract

Spintronics is a viable candidate to become a cornerstone of future computing by exploiting the digital nature and extended coherence of the spin (as opposed to the momentum) for an assembly of electrons. The weak spin-orbit interaction of carbon makes it a bright prospect to take the place of silicon, on which today's consumer electronics are built. Its recently discovered two-dimensional allotrope, graphene, has garnered much attention in the past years with recent papers indicating its utility for spintronics.

This thesis is written on my Master's project study of conduction electron spin resonance (CESR) in potassium doped graphite, a material that was previously shown to be a model system for the electronic structure of biased graphene. It focuses on probing the spin relaxation time and the spin susceptibility in KC_8.

I give an overview of the relevant materials, its literature, magnetic resonance, and in particular of conduction electron spin resonance. The synthesis methods and the implemented setup are also discussed in detail.

Successful experiments were conducted on the applicability of CESR spin susceptibility determination and spin relaxation in KC_8. Values of the temperature dependent line-width and room temperature g-shift were found to be in agreement with the literature data but a much better temperature resolution is presented.

The relation between the value of the g-factor and the homogeneous, i.e. relaxation related ESR line-width agrees with the expectations based on the so-called *Elliott-Yafet* theory of spin relaxation. The result is in harmony with earlier results for metals, which are revisited in this thesis. This result indicates that much as the band structure and the structure of doped graphite is different from usual metals, its spin relaxation properties fit into the more general family of metals. It is argued that the result is relevant for the spin-relaxation mechanism in graphene.

Kivonat

A spintronika, ami az elektronok momentumával szemben az elektronspin digitális természetét és nagy koherenciahosszát hasznosítja, a jövő számítástechnikájának alapjául szolgálhat. A rá jellemző gyenge spin-pálya csatolás révén a szén ideális jelölt spintronikai alkalmazásokra, és hogy a félvezetőiparban a szilícium szerepét átvegye. A grafén, a szén 2004-ben felfedezett kétdimenziós módosulata, amelynek spintronikai alkalmazhatóságát több csoport is kimutatta, különösen biztató alkalmazások szempontjából.

Ezen diplomamunka az elmúlt másfél év önálló laboratóriumi munkájának összefoglalója, mely során a káliummal dópolt grafit (KC_8) vezetési elektronspin-rezonanciáját (CESR) vizsgáltam. Elméleti és kísérleti tanulmányok is megmutatták, hogy ez a tömbi anyag az előfeszített grafén sávszerkezetének modellrendszereként működik. Munkám a spindinamika megértésére és a spin-szuszceptibilitás mérésére koncentrált. Áttekintést adok a vizsgált anyagok irodalmáról, a mágneses rezonanciáról és ezen belül a vezetési elektronspin-rezonanciáról. Részletesen bemutatom a mintaelőkészítés folyamatát, hőmérsekletfüggő mérések összeállítását és méréstechnikai sajátosságait.

Dolgozatom demonstrálja a spin rezonancia alkalmazhatóságát spin-szuszceptibilitás mérésére, emellett betekintést ad a KC_8 spin-dinamikájába. A g-faktor és relaxációból származó, más néven ESR vonalszélesség arányossága a várakozásnak megfelelően a spinrelaxáció ún. *Elliott-Yafet* elméletét követi. Ez az eredmény összhangban van fémekre kapott korábbi eredményekkel, amelyeket a dolgozat áttekint. Kísérleteinknek ezáltal sikerült megmutatni, hogy a káliummal dópolt grafit modellezi a grafén spindinamikáját, és egyértelműen alátámasztani a grafénon végzett spintranszport mérések hasonló eredményeit.

Contents

Chapter 1

Introduction

Electronics and digital technology have become a fundamental part of everday life and have in a sense defined the modern lifestyle of the 21^{st} century. Digital electronics has developed exponentially [1] since its inception in practice some 70 years ago. The technology was revolutionized by the invention of the transistor and the realization of semiconductor integrated circuits, paving the way for microelectronics. As integrated circuits of the present day have already reached the nanometer scale, new and innovative technologies are required to keep up with this trend, especially as the quantum limits of conventional silicon-based electronics are fast approaching. Carbon—residing just above silicon in the periodic table of elements—nanostructures have been suggested [2] to replace silicon as the material of future nanoelectronics and for other promising alternative technologies, just as silicon replaced germanium by the end of the 1960's.

Carbon is one of the most abundant and versatile elements in the universe. Although carbon has been studied for centuries it has not ceased to give scientist new problems and challenges to conquer. The recent discovery of *graphene* [3], the two-dimensional allotrope of carbon has garnered enormous interest from the scientific community. The attention stemming from its unique properties, exotic behavior and a wide array of possible innovative applications culminated in the 2010 Nobel Prize in Physics being awarded for its discovery. One of these future applications which could revolutionize is spin electronics, or simply called *spintronics*[1].

Spintronics [4] is an emerging technology which aims to exploit the inherently digital nature and extended coherence length of the electron spin as opposed to the simple charge transport of conventional electronics. A major advantage of the utilization of spin systems is the prolonged conservation of spin information as the spin relaxation time (T_1) usually dominates the electron momentum relaxation time (τ) by several orders of magnitude. The weak spin-orbit interaction of carbon makes graphene a viable candidate for future spintronics applications, as demonstrated in non-local spin valve experiments [5, 6]. However, the underlying spin relaxation mechanisms are yet to be understood.

---

[1] The term was coined by S. A. Wolf in 1996, as a name for a DARPA initiative for novel magnetic materials and devices.

The investigation of spin transport relies on the study of phenomena where an imbalance in spin state can be achieved, such as spin polarized transport measurements or electron spin resonance (ESR) measurements. In this work, I focus on the latter, where we gather spin relaxation information from conduction electron spin resonance curves.

One way of changing the electronic properties of graphene is to tune its Fermi energy, which can be accomplished by gate voltage or chemical doping. ESR spectroscopy reqiures bulk samples, thus electrostatic biasing is not applicable and only chemical doping is feasible. Although graphite, a three-dimensional allotrope of carbon composed of stacked graphene layers, has been studied for decades [7], studies suggesting chemically doped compounds as model systems [8] resulted in renewed interest. Through intercalation, intercalant layers are wedged between the loosely bound graphene layers. Thus the separation of graphene layers is increased and the Fermi energy of the host material is shifted by the charge transfer from the adatoms resulting in effectively decoupled graphene layers. This bulk model system is ideal for ESR experiments as a doped graphene monolayer would not provide an adequate amount of spins for meaningful studies [9].

In this thesis, I review the theoretical background and results of my work on the investigation of electron spin resonance in graphite intercalation compounds. In Chapter 2, the materials are introduced: graphene and its bulk model systems: graphite intercalation compounds. Chapter 3 gives an overview of the theory and standard problems of conduction electron spin resonance. Details of the sample preparation and experimental setup are provided in Chapter 4. Measurement data and discussion are presented in Chapter 5. The thesis concludes with a short summary of the achieved results in Chapter 6.

Chapter 2

Graphitic compounds

The present chapter reviews the materials of interest. My research was focused on graphite intercalation compounds, a family of bulk model systems for biased graphene. I hoped to gain insight into the spin dynamics of graphene through this material as it was applicable for the experimental technique of ESR, unlike pristine graphene. Particular emphasis is placed on stage I potassium doped graphite which is thoroughly studied herein.

2.1 Graphene

Graphene is the two-dimensional monolayer allotrope of carbon. Although predicted by the celebrated Mermin-Wagner theorem [10] and *ab initio* calculations to be instable[1], it was successfully synthesized for the first time in 2004 [3] by Russian physicists Konstantin Novoselov and Andre Geim at the University of Manchester by micromechanical exfoliation of graphite[2].

Since its discovery, it has been shown to be a host to exotic phenomena such as e.g. Berry's phase and the quantum Hall effect [11, 12], even at room temperature [13]. Although the motion of its charge particles is non-relativistic, it exhibits electronic properties distinctive of a 2D gas of particles which obey the Dirac equation [12] rather than the expected Schrödinger equation. The striking properties of graphene are not limited to the demonstration of relativistic quantum mechanical phenomena in a solid but it has various possible commercial applications like solar cells, heat conductors, displays, and sensors which all retain the mechanical advantages of the monolayer: flexibility, elasticity and durability.

---

[1] This does not take account of the slight three-dimensionality caused by ripples.

[2] Colloquially known as the "scotch tape method".

2.1.1 Structure

Graphene is an atomic sheet of carbon atoms arranged in a honeycomb structure with a distance of $a_{\mathrm{C\text{ - }C}} = 1.42$ Å for nearest-neighbor atoms. This hexagonal configuration can be described as a triangular lattice with a basis of two equivalent atoms per unit cell with the following lattice vectors [14]:

$$\mathbf{a}_1 = \left(\frac{\sqrt{3}}{2}a, \frac{1}{2}a\right), \quad \mathbf{a}_2 = \left(\frac{\sqrt{3}}{2}a, -\frac{1}{2}a\right), \tag{2.1}$$

where $a = |\mathbf{a}_1| = |\mathbf{a}_2| = \sqrt{3}a_{\mathrm{C\text{ - }C}} = 2.46$ Å is the lattice constant. The corresponding reciprocal-lattice vectors are:

$$\mathbf{b}_1 = \left(\frac{2\pi}{\sqrt{3}a}, \frac{2\pi}{a}\right), \quad \mathbf{b}_2 = \left(\frac{2\pi}{\sqrt{3}a}, -\frac{2\pi}{a}\right). \tag{2.2}$$

Figure 2.1 illustrates the structure described in (2.1) and (2.2): the honeycomb lattice and the hexagonal Brillouin zone and its high symmetry points. The K and K' or Dirac points are distinguished points of the Brillouin zone, due to the unique quasiparticle dispersion in their vicinity.

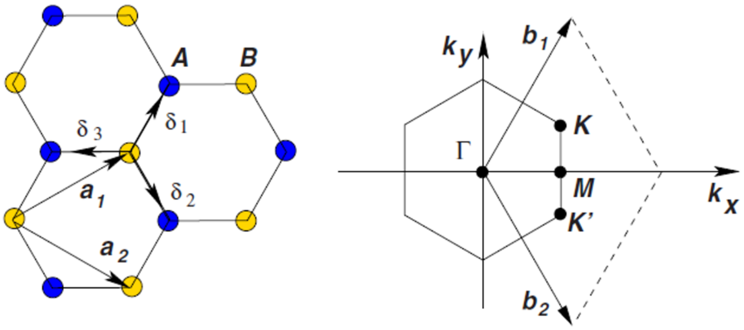

Figure 2.1: *Graphene structure in real (left) and reciprocal space (right) (from [14]). Lattice vectors and the corresponding reciprocal-lattice vectors are denoted as* **a** *and* **b**, *while* δ *refers to nearest neighbor vectors.*

2.1.2 Electronic properties, band structure

The two-dimensionality of graphene is reflected in the atomic bonds as well. The sp^2 hybridization of the in-plane p_x and p_y orbitals with the s orbitals form three covalent σ bonds, responsible for the strong planar structure, described in the preceding section. The covalent bonding of neighboring out-of-plane $2p_z$ orbitals forms the half filled π bands, responsible for most solid state electronic properties [14].

Although calculations for the band structure of graphene have been present for half a century [15], tight-binding models combined with first principle methods yielding more

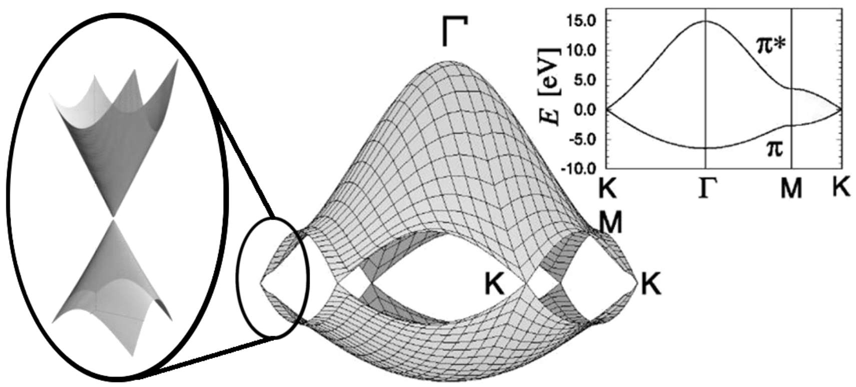

Figure 2.2: *Tight-binding graphene band structure close to the Fermi level (from [18]). Linear dispersion around the Dirac point is magnified (from [14]).*

accurate results are still of great importance [16, 17]. The tight-binding model serves as a good approximation of the band structure shape, with its parameters fitted to experimental data from angle-resolved photoemission spectroscopy and theoretical predictions from ab initio calculations [17]. The tight-binding approximation of the π bands [18] is given by:

$$E^{\pm}(\mathbf{k}) = \frac{\varepsilon_{2p} \mp t w(\mathbf{k})}{1 \mp s w(\mathbf{k})}, \tag{2.3}$$

where $E^{\pm}(\mathbf{k})$ refers to the energy dispersion of the bonding π band $(-)$ and anti-bonding π^* bands $(+)$[3]. ε_{2p}, t and s_0 are the tight-binding parameters. ε_{2p} is the $2p$ orbital energy, $t < 0$ is the hopping integral for nearest-neighbor atoms, and s_0 is the overlap integral for nearest-neighbor atoms. The $w(\mathbf{k})$ function is defined as:

$$w(\mathbf{k}) = \sqrt{3 + 4\cos\frac{\sqrt{3}k_x a}{2}\cos\frac{k_y a}{2} + 4\cos^2\frac{k_y a}{2}}, \tag{2.4}$$

where $a = 2.46$ Å is the lattice constant and k_x and k_y are the components of the $\mathbf{k}$ wave vector. This tight-binding band dispersion is plotted in Fig. 2.2.

The Fermi level is regarded as the zero point of the energy scale, so ε_{2p} is set to 0 eV, while the typical values of the TB parameters are -2.5 eV$> t > -3$ eV for t and $s_0 < 0.1$. The small value of s_0 is responsible for the electron-hole asymmetry of the two bands.

The π and π^* bands touch at the K and K' points. The degeneracy of the two bands and the resulting absence of a band gap is due to the fact that both A and B sites are occupied by carbon atoms. The Dirac points are of particular importance, as they are the apices of the conical dispersion close to the Fermi level, usually referred to as Dirac cones (magnified in Fig. 2.2). This linear dispersion is characteristic of particles following the Dirac equation with zero mass and the quasiparticles are thus called massless Dirac fermions.

---

[3] These are also referred to as valence and conduction bands.

2.2 Graphite

Graphite is a three-dimensional allotrope of carbon composed of stacked graphene layers bound by the van der Waals force. The most commonplace application where this weak interlammellar interaction is exploited is the pencil, for which it has been used since the 16th century. It has also been employed as a lubricant, a battery electrode and a carbon raiser for steelmaking. Despite extensive research in the middle of the previous century, the physics of graphite remains not yet fully understood. The breakthrough of graphene lead to renewed scientific interest in graphite and its compounds.

Layers in graphite are separated by a distance of 3.35 Å. The properties of graphite strongly depend on the stacking order of these layers. For example, if layers are arranged in the so-called AA stacking, so that carbon atoms are above each other, the properties of the bulk graphite are similar to that of the monolayer [19]. The standard arrangement is the AB stacking of layers, usually referred to as Bernal-stacking, shown in Fig. 2.3. In this geometry, graphene layers are shifted so that every second atom of a layer is above a carbon atom or in the center of a hexagon of the other layer.

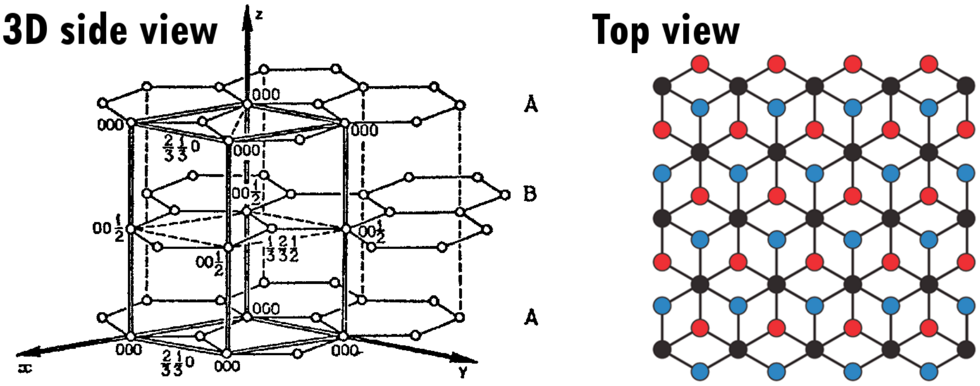

Figure 2.3: *Side (from [7]) and top (from [20]) view of the standard AB Bernal-stacking of graphite. Black circles denote overlapping atoms, while blue and red circles denote the non-overlapping points of the top and bottom layers.*

Graphite can be produced with various crystal sizes and impurity levels, both synthetically or from mined natural graphite. Our research employed high purity powder and highly ordered pyrolitic graphite as host materials. Graphite powder is an ensemble of random orientation graphite microcrystallites.

HOPG is a synthetic form of graphite, produced by the decomposition of a hydrocarbon at high temperature and subsequent heat treatment, often in a pressurized environment. The resulting material is of a lamellar structure, highly oriented along the *c*-axis (mosaic angles less than 1°). Its layer planes are a random collection of crystallites with ~1 mm average diameter and impurity levels on the order of 10 ppm ash or better.

2.3 Graphite intercalation compounds

Graphite intercalation compounds (GICs) [7] are crystalline salts of graphite. Intercalation is a chemical doping procedure where atomic layers of donors or acceptors[4], known as intercalants are wedged between the graphene layers that compose graphite. The resulting compounds possess a similar electronic structure as that of mono- or multilayer graphene with the bands of the doping material mixed in. However the Fermi level is shifted, due to the charge transfer between the carbon atom and the intercalant. This also increases the number of charge carriers, leading to a change in the plasma frequency and consequently a change in the color of the material. E.g. in potassium graphite prepared from HOPG, the metallic gray color of HOPG changes to gold, steel blue or dark blue for stages 1, 2, and 3, respectively [7].

The most important property of GICs is that they form periodic arrays of layers that are thermodynamically stable. This characteristic ordering is known as the *staging phenomenon.* GICs are thus classified into stages, according to the number of graphene layers between two intercalant layers. Fig. 2.4 depicts various stages for a GIC species.

2.4 Potassium graphite

Potassium doped graphite or simply potassium graphite is one of the most well studied GICs. It is described by the KC_x stoichiometry, with $x_1 = 8, x_2 = 24, x_3 = 36, ...$ for stages $n = 1, 2, 3...$, and so on. The layer stacking arrangement is illustrated in Fig. 2.4.

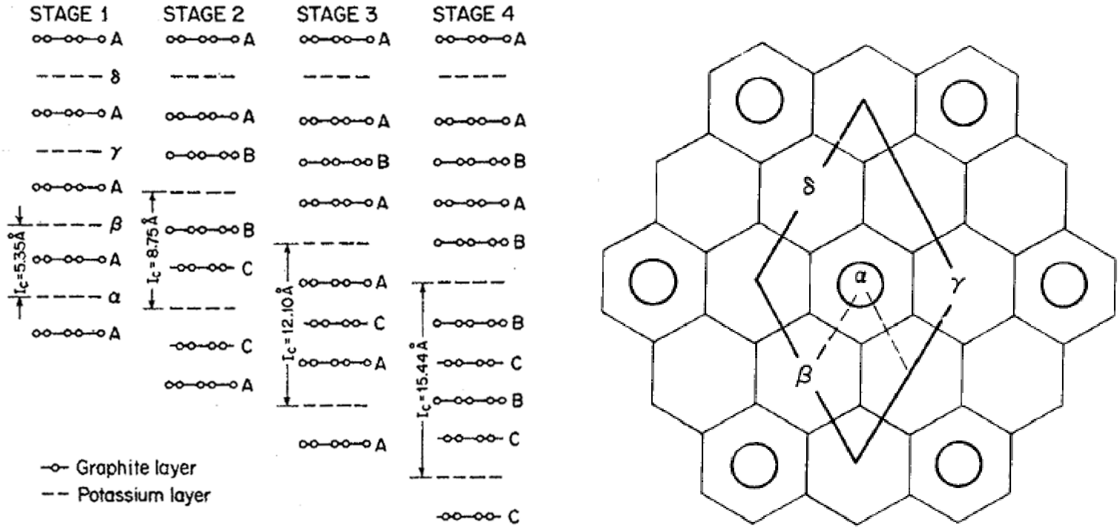

Figure 2.4: *Side (left) illustration of layer stacking in potassium graphite for stages* $1 \geq n \geq 4$ *and top (right) view for stage 1 (from [7])*

---

[4] The mechanism is the same in the case of intercalant molecules.

The period of potassium layers can be written as:

$$I_{\mathrm{c}} = d_{\mathrm{s}} + (n-1)c_0, \tag{2.5}$$

where n is the stage index, $c_0 = 3.35$ Å is the separation of graphene layers, and $d_{\mathrm{s}} = 5.35$ Å is the separation of boundary graphene layers.

In the following, I narrow my scope to the stage 1 compound (KC_8) on which my research was focused on. In this compound, graphene layers are stacked in the AA order with the position of the potassium atoms varying from layer to layer (see Top view in Fig. 2.4). Its conductivity is highly anisotropic with $\frac{\sigma_{ab}}{\sigma_c} = 56$. This material was intensively studied after it was shown to be superconductor at sub-Kelvin temperatures [21] which is not observable in neither graphite nor potassium. However this interest has gradually diminished by the end of the 1980's.

Nowadays, its study is motivated by the enormous interest in graphene, which requires earlier works to be revisited with emphasis on present expectations. Recent studies have shown that it is a model system of biased graphene [8] and that both graphene-derived electrons and graphene-derived phonons are crucial for its superconductivity [22].

Chapter 3

Theory of electron spin resonance

Electron spin resonance (ESR)[1] has become a widespread contact free characterization method since its discovery in the 1940's [23], used in various branches of science from medicine through chemistry to physics. In physics, it is mainly utilized to examine the magnetic interactions or spin-dynamics of unpaired electrons, for which it was used in my research.

In the present chapter, I discuss the theoretical background of this method from the fundamentals to the specifics regarding conductive samples. In order to properly deal with the specifics of conduction electron spin resonance (CESR), we first need to understand the fundamentals of *magnetic resonance*.

3.1 Basics of magnetic resonance

Magnetic resonance refers to the phenomenon of a resonant transition which arises in the presence of a magnetic field. It is based on the Zeeman effect, the splitting of degenerate energy levels when an external magnetic field is applied, which is discussed in Section 3.1.1. As for a classical oscillator, the amplitude of the transition is only significant when the frequency of the excitation matches or is close to that of the resonance. The width of the resonance is governed by the relaxation rate of the excited electrons, which is analogous to the damping of a classical oscillator. The resonance dynamics can be accurately described by empirical equations of motion as it is shown in Section 3.1.2.

3.1.1 The Zeeman effect

Classical electrodynamics states that the magnetic and angular moment of a charged particle are proportional. The same relation holds true for the equivalent quantum mechanical operators:

$$\mathbf{m} = \gamma \hbar \mathbf{L}, \tag{3.1}$$

---

[1] Sometimes referred to as electron paramagnetic resonance

where the proportionality is governed by the $\gamma = \frac{q}{2m}$ gyromagnetic ratio. Consequently, the quantized nature of $\mathbf{L}$ is conserved in the eigenvalues of $\mathbf{m}$. Here, dimensionless $\mathbf{L} = \frac{\widehat{\mathbf{L}}}{\hbar}$ angular momentum operators are used, keeping with the notation of magnetic resonance literature [24]. For a particle of elementary charge, the $\mu_\mathrm{B} = \frac{e\hbar}{2m_e} = 9.274(0) \cdot 10^{-24} \frac{\mathrm{J}}{\mathrm{T}}$ coefficient is the quantum value of the magnetic moment, the *Bohr-magneton*:

$$m_z = \mu_\mathrm{B} l_z, \tag{3.2}$$

The Stern-Gerlach experiment [25] revealed that the electron also possesses an intrinsic quantum number which is coupled to its magnetic moment. As it could be interpreted as the angular moment stemming from an electron spinning around its own axis, the new quantum number was named. However this classical treatment proved inadequate, the origin of the spin was explained by the Dirac equation [26], which became the cornerstone of relativistic quantum mechanics. It showed that for spins, the analog of eq. (3.1) has to be amended by a coefficient of $g_e = 2$, known as the g-factor:

$$\mathbf{m} = \gamma_e \mathbf{S} = -g_e \mu_\mathrm{B} \mathbf{S} \tag{3.3}$$

Here, $\mathbf{S}$ is the dimensionless spin operator and the free electron gyromagnetic ratio (γ_e) is defined as

$$\gamma_e = g_e \frac{q}{2m_e} = g_e \frac{-e}{2m_e} = -g_e \mu_\mathrm{B}, \tag{3.4}$$

where g_e is the free electron g-factor, m_e is the electron mass, and e is the elementary charge. The value of the electron g-factor was later refined by quantum electrodynamics, giving $g_e = 2.00231(9)$. Thus the $\frac{\gamma_e}{2\pi} \approx 28 \frac{\mathrm{GHz}}{\mathrm{T}}$ is obtained.

The energy levels of a system possess a two-fold spin degeneracy in the absence of a magnetic field energy. This degeneracy is lifted upon the application of a non-zero magnetic field, as it designates two inequivalent orientations of the spin with different energies. This is known as the *Zeeman effect.*

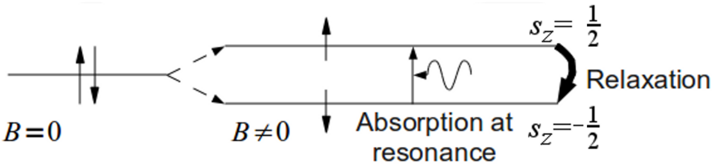

Figure 3.1: *Zeeman splitting of an electron ($S = \frac{1}{2}$) induced by an external magnetic field.*

It can be formulated by introducing the magnetic energy of the $\mathbf{m}$ magnetic moment associated with the $\mathbf{S}$ spin in the Hamiltonian of the system:

$$\mathcal{H}_\mathrm{Zeeman} = -\mathbf{mB} = g_e \mu_\mathrm{B} \mathbf{BS} = g_e \mu_\mathrm{B} B_z s_z. \tag{3.5}$$

The result is a lower energy parallel ($\mathbf{mB} > 0$) and a higher energy antiparallel ($\mathbf{mB} < 0$) configuration, as shown in Fig. 3.1. By substituting the $s_z = \pm\frac{1}{2}$ eigenvalues for the two spin orientations of half-spin electrons we get:

$$\Delta E = \hbar\omega = g_e \mu_\mathrm{B} B_z, \tag{3.6}$$

the level splitting and transition frequency of this two-level system.

3.1.2 The Bloch equations

The phenomenological description of magnetic resonance was introduced by Felix Bloch [27] in 1944 by formulating the macroscopic behavior of the $\mathbf{M}$ magnetization by the means of classical electrodynamics. The equations describe the $\omega_\mathrm{L} = \gamma_e B_0$ angular frequency Larmor precession of $\mathbf{M}$ around a z-axis magnetic field with $\mathbf{M}$ asymptotically converging into the equilibrium position of $\mathbf{M}_0 \parallel z$ on a time scale characteristic of the exponential z-axis relaxation.

$$\frac{dM_z(t)}{dt} = \gamma_e[\mathbf{M} \times \mathbf{B}]_z + \frac{M_0 - M_z(t)}{T_1} \tag{3.7}$$

Analogously the x, y components will vanish ($M_{x,y} = 0$) on a timescale representing the in-plane loss of the magnetization.

$$\frac{dM_x(t)}{dt} = \gamma_e[\mathbf{M} \times \mathbf{B}]_x - \frac{M_x(t)}{T_2} \tag{3.8}$$

$$\frac{dM_y(t)}{dt} = \gamma_e[\mathbf{M} \times \mathbf{B}]_y - \frac{M_y(t)}{T_2} \tag{3.9}$$

Equations (3.7), (3.8), and (3.9) are the so-called *Bloch equations*. Generally, the T_1 (*spin-lattice* or *longitudinal*) and T_2 (*spin decoherence* or *transversal*) relaxation times are not equal. However in metals they are equal ($T_1 = T_2$) [4].

By solving these equations for a $\mathbf{B}$ field composed of a $\mathbf{B}_0$ static external field and small $\mathbf{B}_1(\omega)$ alternating excitation field [24], the magnetization is obtained. The steady state solution for the x and y magnetization is given in a reference frame rotating at ω.

$$M'_x = \frac{1}{\mu_0}\chi_0\omega_0 T_2 \frac{(\omega_0 - \omega)T_2}{1 + (\omega_0 - \omega)^2 T_2^2} B_1 \tag{3.10}$$

$$M'_y = \frac{1}{\mu_0}\chi_0\omega_0 T_2 \frac{1}{1 + (\omega_0 - \omega)^2 T_2^2} B_1 \tag{3.11}$$

Here, the rotating frame is denoted as $'$, $\omega_0 = \gamma_e B_0$ is the transition frequency, and the equilibrium magnetization is formulated as $M_0 = \frac{\chi_0 B_0}{\mu_0}$, as a function of the χ_0 static spin susceptibility.

The solution in the standing reference frame of the laboratory is

$$M_x(t) = M'_x \cos(\omega t) + M'_y \sin(\omega t) = (\chi' \cos(\omega t) + \chi'' \sin(\omega t))B_{x_0} = \chi B_x(t), \qquad (3.12)$$

where the time dependent response is simplified by the introduction of a complex χ susceptibility:

$$\chi = \chi' - i\chi'', \qquad (3.13)$$

The transition is caused by a circularly polarized field [24, 27], which is only one component of the applied B_x linearly polarized field, hence $B_{x_0} = 2B_1$. Thus, the real (χ') and imaginary (χ'') parts are given by

$$\chi'(\omega) = \frac{\chi_0}{2}\omega_0 T_2 \frac{(\omega_0 - \omega)T_2}{1 + (\omega - \omega_0)^2 T_2^2} \quad \text{and} \qquad (3.14)$$

$$\chi''(\omega) = \frac{\chi_0}{2}\omega_0 T_2 \frac{1}{1 + (\omega - \omega_0)^2 T_2^2}, \qquad (3.15)$$

and shown in Fig. 3.2.

The real and imaginary parts of the susceptibility describe the elastic and dissipative response of the system, i.e. the dispersion and absorption of the electromagnetic waves, respectively. These are connected by the Kramers-Kronig relation.

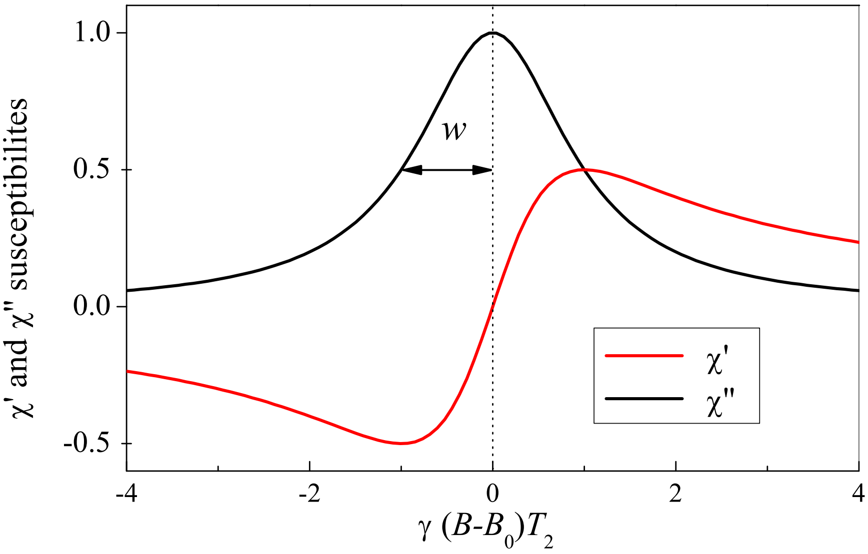

Figure 3.2: *The real and imaginary parts of the susceptibility as a function of its dimensionless argument.*

The solution presented in (3.14) and (3.15) is applicable to nuclear magnetic resonance (NMR). The instrumentation of ESR spectroscopy (see Sec. 4.2) involves sweep of the magnetic field, while keeping the excitation frequency constant and it employs a detection scheme that measures the derivative of the absorption. Therefore resonances manifest as derivative Lorentzian curves as a function of the external field:

$$f(B) = I \cdot \frac{dL(B)}{dB} = I \frac{1}{\pi} \frac{-2w}{\left(w^2 + (B - B_0)^2\right)^2}, \tag{3.16}$$

where I is the intensity of the normalized $L(x)$ $\left(\int\limits_{-\infty}^{\infty} L(x)dx = 1\right)$ Lorentzian function with w line-width.

The parameters of the resonance curve can be obtained by comparing (3.15) and (3.16). The static spin susceptibility appears in the I intensity parameter, the second integral of the curve[2]:

$$I = \frac{\pi}{2} B_0 \chi_0 \tag{3.17}$$

The w line-width is inversely proportional to the T_2 xy-plane spin dephasing time:

$$w = \frac{1}{\gamma T_2} \tag{3.18}$$

The third important parameter of the curve is the resonance field, from which the g-factor can be calculated. The magnetic field acting on unpaired electron of the sample is a local B_{loc} field, the B_0 external field supplemented by the field of the electrons and nuclei of the sample. This is detected as an apparent resonance field, different from what we would expect for free electrons, and treated as a $g = g_e \xi$ departure from $g_e = 2.0023$:

$$\hbar\omega = \Delta E = g_e \mu_{\text{B}} B_{\text{loc}} = g_e \mu_{\text{B}} (B_0 \xi) = (g_e \xi) \mu_{\text{B}} B_0 = g \mu_{\text{B}} B_0 \tag{3.19}$$

3.2 Spin susceptibilities

The ESR signal is proportional to the susceptibility of the measured sample. This section summarizes the relevant static spin susceptibilities [28] in the materials studied herein.

Materials composed of non-interacting unpaired electrons will act as an ensemble of independent magnetic moments. The magnetization of such materials can be formulated by the means of statistical physics. This yields a magnetization of:

$$\langle M \rangle = \frac{N}{V} g_J \mu_{\text{B}} J B_J \left(\frac{g_J \mu_{\text{B}} B_0 J}{k_{\text{B}} T} \right) \tag{3.20}$$

where g_J is the Landé g-factor, J is the total angular momentum quantum number, and $B_J(x)$ is the so-called *Brillouin-function*:

---

[2] This is the area under the Lorentzian curve of the resonance

$$B_J(x) = \frac{2J+1}{2J} \coth\left(\frac{2J+1}{2J}x\right) - \frac{1}{2J} \coth\left(\frac{1}{2J}x\right) \tag{3.21}$$

We operate far from the saturation of the magnetization, so we shall consider the case of $B_0 \to 0$ external field. We arrive at the expression of

$$\chi_0^{\text{Curie}} = \mu_0 \lim_{B_0 \to 0} \frac{M_0}{B_0} = \mu_0 \frac{S(S+1)g^2\mu_{\text{B}}^2}{3k_{\text{B}}T} \frac{1}{V_C}, \tag{3.22}$$

which is known as the *Curie susceptibility.* Eq. (3.22) is inversely proportional to the $V_C = \frac{V}{N}$ unit cell volume, and the temperature, T. Note that J has been replaced by S as the L orbital momentum will be quenched [24] for studied materials of Curie susceptibility.

Our research was focused on conductive samples. The paramagnetism of the unbound electrons is qualitatively different from that of the localized spins. Electrons obey the Fermi-Dirac distribution:

$$f(\varepsilon) = \frac{1}{e^{\beta(\varepsilon - \mu_c)} + 1}. \tag{3.23}$$

When a magnetic field is applied, the Fermi level of the spin-up and spin-down configurations will be shifted by equal values but in the opposite direction. It results in a small surplus of one spin species. This paramagnetic moment is generated by the electrons close to the Fermi energy, thus the susceptibility will be proportional to the Fermi energy density of states:

$$\chi_0^{\text{Pauli}} = \frac{1}{4} g_e^2 \mu_0 \mu_{\text{B}}^2 g(E_{\text{F}}) \frac{1}{V_C} \tag{3.24}$$

where $g(E_{\text{F}})$ is the atomic density of states at the Fermi energy. Eq. (3.24) is referred to as the Pauli susceptibility and is usually two orders of magnitude smaller than the Curie susceptibility.

3.3 Conduction electron spin resonance

The experimental and theoretical investigation of electron spin resonance in metals was pioneered in the early half of the 1950's by the group of Arthur Kip and Charles Kittel [29] at Berkeley with theorists working alongside them such as Freeman Dyson and Yako Yafet. After preliminary calculations for the g-factor shift of sodium [30], the group successfully observed the spin resonance of the conduction in metallic sodium [31]. This result was only the forerunner of later results wchich provided theories explaining the underlying physics. Dyson explained the anomalous absorption curve [32, 33], while Elliott's consideration of the spin orbit shed light on the spin relaxation mechanism of metals and semiconductors [34], the results of both will be reviewed in Sections 3.3.2 and 3.4, respectively. These treatises paved the way for spin resonance studies in conductive samples, broadly termed as conduction electron spin resonance (CESR).

3.3.1 The skin effect

In order to understand the response of conduction electrons, the penetration of microwaves in a conductive sample has to be considered.

According to Ohm's law the free current density is proportional to the electric field:

$$\mathbf{j}_f = \sigma \mathbf{E} \tag{3.25}$$

with a coefficient of σ, the conductivity.

To look for a steady state solution without any accumulated surface charge density, we fix $\rho_f = 0$. This is in accordance with $\nabla \mathbf{j}_f = -\frac{\partial \rho_f}{\partial t}$, the continuity equation of the free charge density.

With these conditions, Maxwell's equations take the following form:

$$\nabla \cdot \mathbf{E} = 0 \tag{3.26}$$

$$\nabla \cdot \mathbf{B} = 0 \tag{3.27}$$

$$\nabla \times \mathbf{E} = -\frac{\partial \mathbf{B}}{\partial t} \tag{3.28}$$

$$\nabla \times \mathbf{B} = \mu \mathbf{E} + \mu \varepsilon \frac{\partial \mathbf{E}}{\partial t} \tag{3.29}$$

Applying curl to (3.28) and (3.29), we arrive at a modified wave equation for the conductive medium:

$$\nabla^2 \mathbf{B} = \mu_0 \epsilon_0 \frac{\partial^2 \mathbf{B}}{\partial t^2} + \mu \sigma \frac{\partial \mathbf{B}}{\partial t}. \tag{3.30}$$

We shall solve this with a plane wave ansatz of

$$\mathbf{B}(z,t) = \mathbf{B}_0 e^{i(kz-\omega t)} \tag{3.31}$$

which yields an unmodified ω and a complex wave vector of

$$\tilde{k} = \sqrt{\mu \varepsilon \omega^2 + i \mu \sigma \omega} = k + i\kappa, \tag{3.32}$$

which can be written as the sum of a real (k) and an imaginary part (κ), which are defined as

$$k = \frac{2\pi}{\lambda} = \omega \sqrt{\frac{\varepsilon \mu}{2}} \left[\sqrt{1 + \left(\frac{\sigma}{\omega \varepsilon} \right)^2} + 1 \right]^{\frac{1}{2}}, \text{ and} \tag{3.33}$$

$$\kappa = \frac{1}{\delta} = \omega \sqrt{\frac{\varepsilon \mu}{2}} \left[\sqrt{1 + \left(\frac{\sigma}{\omega \varepsilon} \right)^2} - 1 \right]^{\frac{1}{2}}. \tag{3.34}$$

The result is an attenuated wave,

$$\mathbf{B}(z,t) = \mathbf{B}_0 e^{-\frac{z}{\delta}} e^{i(kz-\omega t)}, \tag{3.35}$$

with its amplitude decreasing exponentially as a function of z. The δ length scale of the attenuation—defined in (3.34)—is known as the *skin depth.*

This behavior is depicted in Fig. 3.3. For a highly conductive medium, the wavelength of the incident microwave is several orders of magnitude greater than in the medium, where $\lambda \approx 2\pi\delta$.

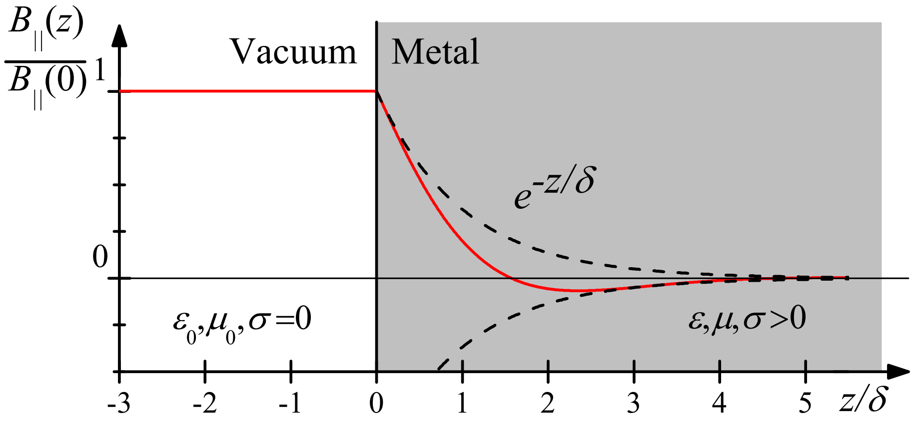

Figure 3.3: *Illustration of the skin effect. The magnitude of the alternating magnetic field decreases exponentially on a length scale of* δ*. Note the severe decrease in wavelength for the conductive medium.*

The complex wave vector will also result in a ϕ phase difference for the penetrating electric and magnetic fields.

$$\phi = \tan^{-1}\frac{\kappa}{k} \tag{3.36}$$

3.3.2 The Dysonian line shape

The previous section showed that for conductive samples, the alternating microwave field will penetrate only skin depth. This leads to an anomalous absorption derivative ESR signal [32]. The line shape of conductive samples was formulated by Dyson [33], hence they are referred to as Dysonian lines.

Dyson considered that although electrons are only excited within the penetration depth, their diffusion is not limited to it. Electrons can diffuse in and out of the skin depth, resulting in a rather complex response of the material. Correspondingly, the line shape will be described as a function of the usual parameters of the g-factor, the static spin susceptibility (χ), spin relaxation time (T_2) and the newly included parameters of R and λ. These parameters are defined as

$$R = \sqrt{\frac{T_\mathrm{D}}{T_2}}, \tag{3.37}$$

the square root of the ratio of the electron diffusion time across the skin depth (T_D) and the spin relaxation time (T_2), and

$$\lambda = \frac{d}{\delta}, \tag{3.38}$$

the ratio of the sample size (d) and the skin depth (δ).

The detected signal is the frequency derivative[3] of the real part of a rather elaborate complex formula, and can be written as [35]:

$$\frac{dP}{d\omega} = N\left\{\mathrm{Re}(F^2)\,\mathrm{Re}\left[\frac{dG(\omega-\omega_0)}{d\omega}\right] - \left[\mathrm{Im}(F^2)\,\mathrm{Im}\,\frac{dG(\omega-\omega_0)}{d\omega}\right]\right\} \tag{3.39}$$

where F is a function of u, which are defined as

$$F = -u\tan(u) \tag{3.40}$$

$$u = \frac{\lambda}{2}(1+i). \tag{3.41}$$

The $G(\omega-\omega_0)$ is defined as[4]

$$G(\omega-\omega_0) = \frac{i}{(w^2-u^2)}\left[2u^2\frac{\cot(w)}{w} + (w^2-3u^2)\frac{\cot(u)}{u} + (w^2-u^2)\mathrm{cosec}^2(u)\right], \tag{3.42}$$

where

$$w = \frac{\lambda R}{2}(\xi + i\eta) \tag{3.43}$$

is a function of

$$\xi = [sgn(x)][(1+x^2)^{\frac{1}{2}} - 1]^{\frac{1}{2}}, \quad \text{and} \tag{3.44}$$

$$\eta = [(1+x^2)^{\frac{1}{2}} + 1]^{\frac{1}{2}}, \tag{3.45}$$

which bear an argument of

$$x = (\omega-\omega_0)T_2. \tag{3.46}$$

Simulated Dysonian curves are plotted in Fig. 3.4 for different R ratios. Note that as the the ratio increases, so does the asymmetry of the derivative line, resulting in an extreme case where the signal resembles a Lorentzian curve instead of a derivative Lorentzian.

This formula is rather hard to comprehend or even try to give it a simple interpretative picture. Before computer assisted data analysis, such lines were evaluated by

---

[3] As for the Bloch equations, the response is formulated as a function of the ω excitation and ω_0 resonance frequencies.

[4] This function differs in a factor of i in Refs. [33] and [35], here we adopt the function in Dyson's original paper [33].

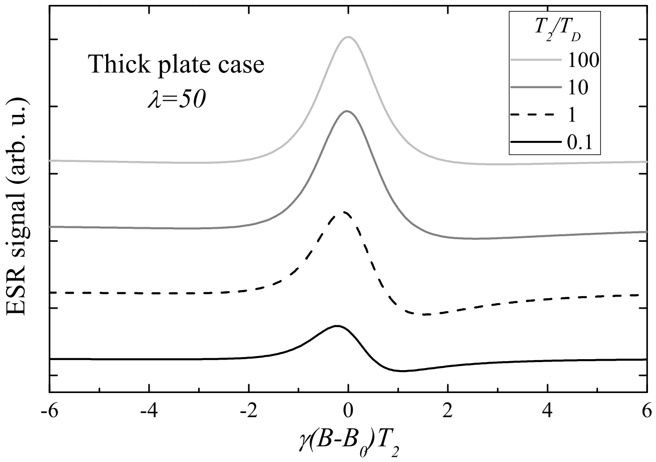

Figure 3.4: *Simulated derivative Dysonian curves for the case of an extremely thick slab ($\lambda = 50$). Curves are plotted for various ratios of the spin relaxation (T_2) and electron diffusion (T_D) times*

reading the asymmetry of the line and the apparent line-width and resonance field off an oscilloscope or printed curve. This of course resulted in somewhat unpredictable results. With the help of computers, evaluation got much easier and allowed curve fitting. It was shown that Dysonian lines of moderate asymmetry could be fitted with a combination of derivative absorption and dispersion Lorentzian curves [35]. This allowed the quick and robust evaluation of curves. It should be noted that with today's computing power, curves could be fitted with numerically simulated Dysonian curves, however the large number of parameters makes this method somewhat instable.

3.4 The Elliott-Yafet theory

Dyson's treatise explained the line shape for conduction electrons, however the physics behind the relaxation times was yet to be uncovered. Elliott [34] showed for isotropic semiconductors and metals that the dominant process is the spin-flip scattering of conduction electrons by acoustic phonons, and the process is governed by the spin-orbit interaction. Elliott's results were later systematically amended by Yafet [36]. It was originally devised for the very specific goal of explaining the "Theory of the Effect of Spin-Orbit Coupling on Magnetic Resonance in Some Semiconductors", as it is stated in the title of Elliott's paper however the spin relaxation mechanism it introduced became one of the cornerstones of spintronics. The following paragraphs present the main points and results of the theory [4, 34, 36].

To determine the effect of the spin-orbit coupling, we consider its Hamiltonian :

$$\mathcal{H}_{\mathrm{SO}} = \frac{\hbar}{4m^2c^2}(\nabla V \times \mathbf{p})\mathbf{S}, \tag{3.47}$$

where m is the free electron mass, V is the scalar potential with no spin dependent terms, $\mathbf{p}$ is the linear momentum operator and $\mathbf{S}$ is the spin operator. Bloch states of a single spin configuration will not be eigenstates of the spin operator. Treating the $\mathcal{H}_{\mathrm{SO}}$ term as a perturbation, we attain an admixture of spin-up and spin-down Bloch states with $\mathbf{k}$ lattice momentum.

$$\Psi_{\mathbf{k},\uparrow}(\mathbf{r}) = \left(a_{\mathbf{k}}(\mathbf{r})\left|\uparrow\right\rangle + b_{\mathbf{k}}(\mathbf{r})\left|\downarrow\right\rangle\right) e^{i\mathbf{kr}} \tag{3.48}$$

$$\Psi_{\mathbf{k},\downarrow}(\mathbf{r}) = \left(a^*_{-\mathbf{k}}(\mathbf{r})\left|\downarrow\right\rangle + b^*_{-\mathbf{k}}(\mathbf{r})\left|\uparrow\right\rangle\right) e^{i\mathbf{kr}} \tag{3.49}$$

$$\Psi_{\mathbf{k},\uparrow}(\mathbf{r}) = u_{\mathbf{k}}(\mathbf{r})\left|\uparrow\right\rangle e^{i\mathbf{kr}} \tag{3.50}$$

$$\Psi_{\mathbf{k},\downarrow}(\mathbf{r}) = \left(a^*_{-\mathbf{k}}(\mathbf{r})\left|\downarrow\right\rangle + b^*_{-\mathbf{k}}(\mathbf{r})\left|\uparrow\right\rangle\right) e^{i\mathbf{kr}} \tag{3.51}$$

where $a_{\mathbf{k}}$ and $b_{\mathbf{k}}$ lattice-periodic coefficients which reflect the symmetry properties of the solid, like the $u_{\mathbf{k}}$ function of Bloch states. $\mathcal{H}_{\mathrm{SO}}$ couples electron states of opposite spins, same $\mathbf{k}$, but different bands. The perturbation treatment yields $a_{\mathbf{k}}, b_{\mathbf{k}}$ coefficient of:

$$|a| \approx 1, \quad \text{and} \quad |b| \approx \frac{\lambda}{\Delta E} \tag{3.52}$$

where λ is the matrix element of the spin-orbit term[5] for the conduction and a near-lying band of the same $\mathbf{k}$, and ΔE is the energy separation of the aforementioned bands. The admixture ratio is dependent of the spin-orbit interaction strength which scales as Z^4 (Z is the atomic number) and the shape of the Fermi surface.

Elliott estimated the g-factor shift to be in the order of magnitude of the admixture.

$$\Delta g = g - g_e = \alpha_1 \frac{|b_{\mathbf{k}}|}{|a_{\mathbf{k}}|} = \alpha_1 \frac{\lambda}{\Delta E}, \tag{3.53}$$

where $g_e = 2.00231(9)$ is the free electron g-factor, $\alpha_1 = 1..10$ is a constant over unity, determined by the band structure.

The spin-orbit alone does not induce spin flipping and spin relaxation, it is only responsible for inducing the mixed spin-state. The spin-flip scattering stems from the same interaction Hamiltonian as for momentum scattering with no spin-flip. Impurities produce a constant, temperature independent term in $\frac{1}{\tau}$, it is responsible for the residual resistivity. The contribution of phonons is given by the so called Bloch-Grüneisen curve, which is linear for high temperatures and follows a T^5 dependence well below the Debye temperature.

Using Fermi's golden rule for the mixed spin-state Bloch-type wave functions we defined in (3.50) and (3.51), the momentum relaxation time, characteristic of scattering

---

[5] This should not be confused with the spin-orbit constant

is given by

$$\frac{1}{\tau} \propto \left| \int a^*_{\mathbf{k}'} \mathcal{H}_{int} a_{\mathbf{k}} e^{i(\mathbf{k}-\mathbf{k}')\mathbf{r}} dt \right|^2, \tag{3.54}$$

while the spin relaxation time, characteristic of spin-flipping is given by

$$\frac{1}{T_1} \propto \left| \int (a_{-\mathbf{k}'} \mathcal{H}_{int} b_{\mathbf{k}} - b_{-\mathbf{k}'} \mathcal{H}_{int} a_{\mathbf{k}}) e^{i(\mathbf{k}-\mathbf{k}')\mathbf{r}} dt \right|^2. \tag{3.55}$$

This yields the following relation between the relaxation times:

$$\frac{1}{T_1} = \alpha_2 \frac{|b_{\mathbf{k}}|}{|a_{\mathbf{k}}|} = \alpha_2 \left(\frac{\lambda}{\Delta E} \right)^2 \frac{1}{\tau} \tag{3.56}$$

where α_2 is a band structure dependent constant in the order of unity.

Although the proportionality to the resistivity the ESR line-width:

$$w \propto \frac{1}{T_1} \propto \rho, \quad \text{because} \quad \rho \propto \frac{1}{\tau} \tag{3.57}$$

might seem straightforward, it is not trivial for the whole of the temperature dependence. The connection between the temperature dependence of $\frac{1}{T_1}$ an that of the resistivity was unambiguously proven by Yafet [36], thus

$$\frac{1}{T_1}(T) \propto \langle b \rangle^2 \rho(T), \tag{3.58}$$

is known as the Yafet relation.

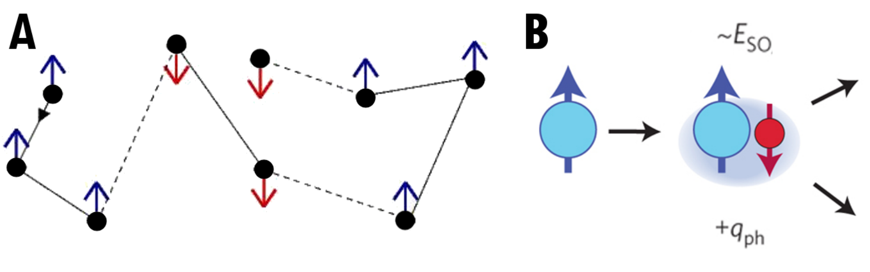

Figure 3.5: *Schematics of the Elliott-Yafet spin relaxation mechanism. Left* (**A**)*: The evolution of the electron spin during transport (from [37]). Right* (**B**)*: The spin scattering process. The spin-orbit interaction induces an admixture of spin-up and spin-down states, which occasionally leads to a spin flip (from [38]).*

The attained spin relaxation mechanism is illustrated in Fig. 3.5. Inset A illustrates the propagation of the spin, with spin flips occurring only if momentum scattering occurs. Inset B shows that the SO coupling forms a mixed spin state, which allows the momentum scattering interaction term to induce spin flipping with a small probability.

This theory [34, 36] explained the CESR for most pure metals [39, 40]. Its validity was shown in a generalized form for one-dimensional metals [41]. Consideration of the shape of the Fermi surface in polyvalent metals resulted in the *"spin hot spot model"* [42, 43]. A generalized approach explained the CESR behavior of strongly correlated metals such as MgB_2 [44], K_3C_{60}, and Rb_3C_{60} [45], where the $\frac{\hbar}{\tau}$ scattering rate is in the order of the ΔE band separation.

Chapter 4

Sample preparation and experimental setup

This chapter discusses the technical details of graphite intercalation, sample handling, as well as the experimental setup used for temperature dependent conduction electron spin resonance spectroscopy.

4.1 Sample preparation

Alkali doped graphite samples were prepared from 3 mm diameter disks of grade I HOPG (SPI Supplies) and high purity fine powder graphite (Fisher Scientific).

The powder samples, although finely ground, formed larger granules upon doping. The formation of macroscopic metallic clusters was unfavorable as microwave penetration was limited to the skin depth as in the HOPG samples. To counter the conglomeration of the powder samples and allow efficient microwave penetration, the graphite was mixed together with an equal mass of a dilute (1.5 ppm) mixture of manganese and magnesium-oxide (Mn:MgO) prior to doping. The ESR-silent and doping insensitive MgO performed the separation of the graphite crystallites, while Mn^{2+} had the added benefit of being a g-factor and susceptibility standard.

Prior to intercalation, the graphite samples were vacuum annealed at $500\,^\circ C$ in a quartz tube. Afterwards samples were handled in an argon filled glove box (Fig. 4.1E) to avoid exposure to oxygen and water. Alkali metals were heated to temperatures above their melting point (typically $120°C < T < 150°C$), upon melting they were soaked into small glass capillaries in which they solidified after cooling. The sample and the capillary of alkali metal were vacuum sealed quartz doping ampoule (Fig. 4.1A & 4.1B). Doping was achieved through two-zone vapor transport intercalation [7], which is explained in the following. Abundant amounts of alkali were used to ensure saturation doping. The resulting compounds (e.g. Fig. 4.1C & 4.1D) were transferred from the doping vessel to a clean quartz tube in the inert atmosphere of the glove box and sealed under helium for the measurements with a pressure of 20 mbar. As described in Section 2.3, doping modifies color of the HOPG samples, attesting its success. In the case of stage 1 and stage 2 potassium graphite, to gold (Fig. 4.1C) and blue (Fig. 4.1D), respectively. In some cases for the stage 1 species, the brief exposure to Ar induces a slight surface dedoping, which is seen from the change in the color of the samples from gold to red, however this does not modify our results significantly, as the bulk of the material remains unchanged.

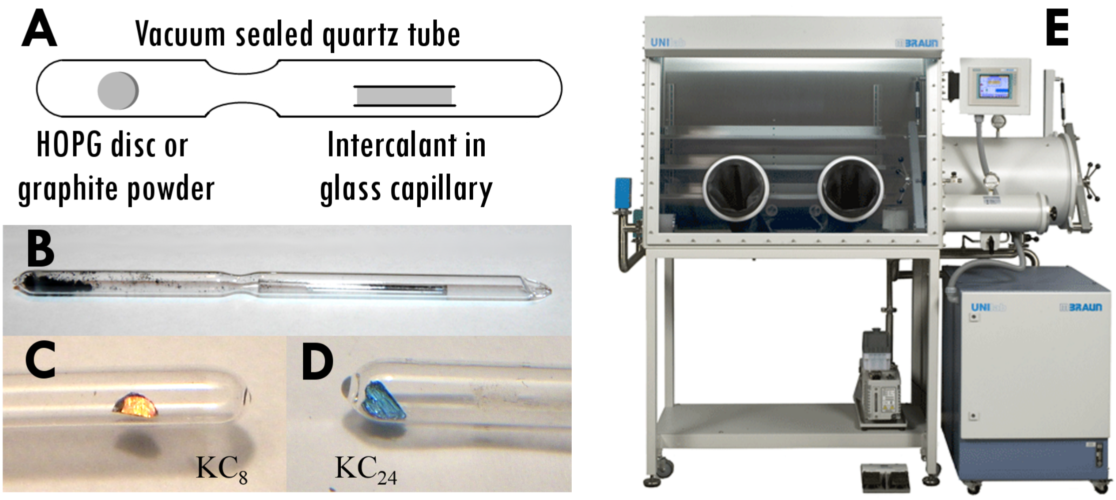

Figure 4.1: *Key elements of sample preparation: illustration* (**A**) *and photograph* (**B**) *of quartz sample holder for doping, which is narrowed to separate the two materials; synthesized stage 1* $\mathrm{KC_8}$ (**C**) *and 2* $\mathrm{KC_{24}}$ (**D**) *potassium doped HOPG compunds after transfer, with distinctive gold and metallic blue colors; MBRAUN Unilab inert gas glove box* (**E**) *operated with* Ar *atmosphere.*

The two-zone vapor method requires the temperature of the graphite host and the intercalant to be independently adjusted, this relies on the spatial separation of the two materials. The intercalant is heated to T_i temperatures thus allowing the alkaline vapor to condense in the graphite (T_g) and form a crystalline salt. By increasing the temperature gradient between the sample and the dopant, higher stages become thermodynamically more stable thus the staging phenomenon can be controlled. The temperature gradients for alkali metals are well documented in Ref. [7] and served as the basis of our synthesis as well. Their typical values for the studied K, Rb and Cs intercalants are given in Table 4.1.

Table 4.1: *Temperature gradients for alkaline two-zone vapor doping (stages* $1 < n < 3$*)*

	K	**Rb**	**Cs**
	$T_\mathrm{i} = 250\,^\circ\mathrm{C}$	$T_\mathrm{i} = 208\,^\circ\mathrm{C}$	$T_\mathrm{i} = 194\,^\circ\mathrm{C}$
Stage	$T_\mathrm{g}(^\circ\mathrm{C})$		
1	225-320	215-330	200-425
2	350-400	375-430	475-530
3	450-480	450-480	550

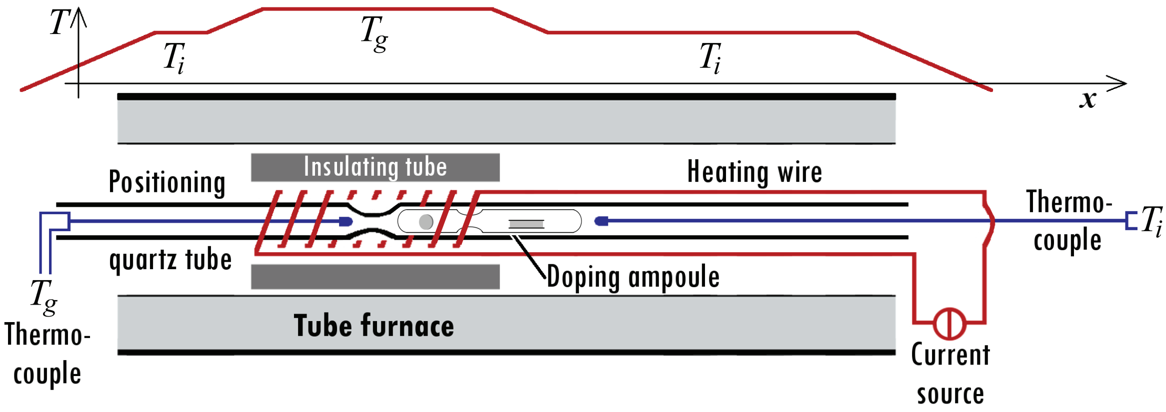

Figure 4.2: *Schematic diagram of the implemented two-zone intercalation setup and its temperature profile, illustrated in the top plot.*

Fig. 4.2. shows the two-zone doping setup assembled as part of the thesis project and used for sample synthesis. In our setup, the separation of the two materials was achieved with the use of inexpensive, home-made doping ampoules: long quartz diameter tubes(ø4 mm) with a middle section narrowed with the use of an oxyacetylene blow torch. The setup is based on the local heating of the graphite host. A ø10 mm quartz tube is placed in a tube furnace which sets the T_i temperature. The surplus heating, needed for a higher T_g is achieved with a Joule heating coil, powered by a controllable voltage source. The resistive heater wire is wrapped around a narrowed section of the tube which ensures the proper placement of the sample. The coil is surrounded by an insulating ceramic tube to prevent significant radiative heat loss. The T_i and T_g temperatures at the two ends of the ampoule are measured with two thermocouples. Thermal insulation fabric was added to the openings of the furnace ensuring thermal stability.

4.2 ESR spectrometer setup

In this section, I present the operating principles of a standard X-band ESR spectrometer, which was the instruments of choice for my research. Afterwards the specifics of the measurements will be discussed. The schematics of the high field ESR is discussed, where some of the experiments were performed.

4.2.1 X-band ESR

Experiments at 9 GHz were carried out using two X-band ESR spectrometers. Temperature dependent measurements in the 100-600 K range were performed on a modified JEOL spectrometer optimized for highly conductive samples, while the low temperature range of 4-250 K was covered with a commercial Bruker Elexsys E500 in the laboratory of Prof. László Forró at the EPFL.

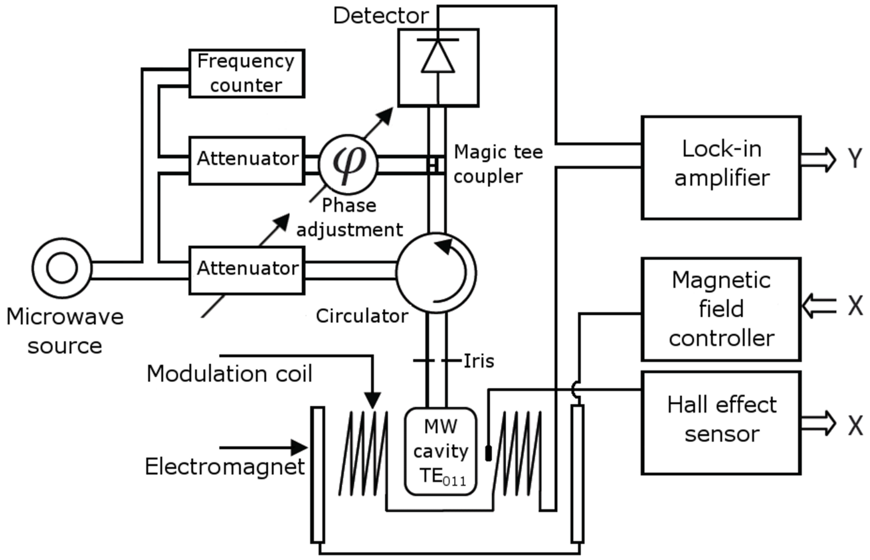

Figure 4.3: *Schematic diagram of the ESR spectrometer*

Figure 4.3. depicts the layout of an X-band ESR spectrometer. This reflection geometry measures the power reflected from the microwave cavity containing the sample, indirectly gathering information from the absorption process.

First, the elements of the microwave bridge are discussed. A tunable frequency microwave source provides the electromagnetic excitation. Its output is split into 3 paths, one connected to the cavity, a second as a reference arm for the detector and a miniscule portion of the waves is coupled into a microwave frequency counter. The first arm is connected to a microwave cavity via waveguides. The power of the incident waves can be adjusted using a tunable attenuator. Microwaves going to and coming form the cavity are separated with a *circulator*, a non-reciprocal three-port terminal in which the reflected wave is transmitted to a different port than the incident wave, thus directing only the reflected radiation to the detector.

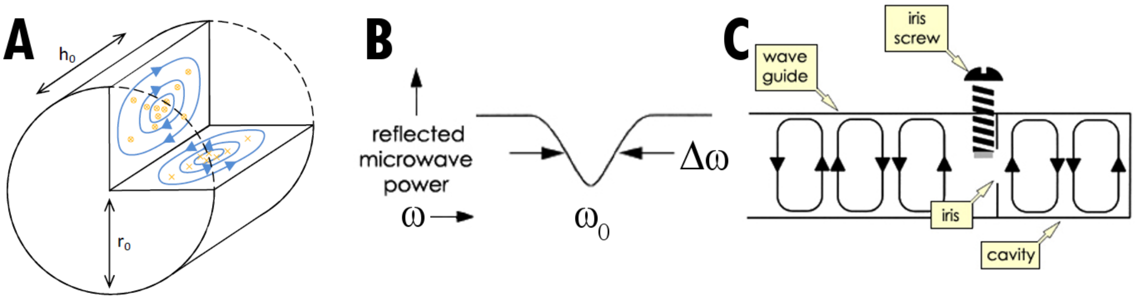

Figure 4.4: *Details of the cavity: Cavity geometry [46] (A), cavity resonance [47] (B), iris for cavity impedance adjustment [47] (C).*

The cylindrical cavity determines a TE_{011} standing wave mode for the alternating field inside. As it is shown in Fig. 4.4A, this arrangement gives a linearly polarized magnetic field for excitation and also separates the electric and magnetic components in space. The cavity resonator acts as an amplifier for the phenomenon we wish to observe, for maximum effect the frequency of the excitation has to match that of the resonance[1]. At resonance, the power absorbed by the cavity and the alternating field inside are maximal (Fig. 4.4B). As slight variation of this condition ruins the experiment, it is critical to remain in resonance. This is achieved with a automatic frequency control (AFC) circuit in the microwave bridge. The efficiency of this negative feedback is determined by the quality factor of the resonator, which has the following two equivalent definitions:

$$Q = 2\pi \frac{E_{\text{energy stored}}}{E_{\text{energy dissipated in one period}}} = \frac{\omega_0}{\Delta\omega} \tag{4.1}$$

The amount of photons reflected from and entering the cavity can be adjusted with the so-called *iris* element of the cavity which tunes the impedance of the waveguide and resonator. For optimal operation there is no reflection at resonance, this is the so-called critical coupling [48].

The microwave of the reference arm is additively mixed with the microwave reflected from the cavity by a magic tee coupler. The phase of the reference arm is adjusted to reach maximum constructive interference. The reference signal does not affect the signal of the cavity, it only adds a constant (DC) term to the incident power on the detector. This acts as a bias to set the semiconductor diode detector to its operating point to ensure optimal sensitivity.

A water-cooled external electromagnet is used to induce Zeeman splitting. As shown previously, electron spin resonance occurs when the energy of the excitation photons matches that of the induced level splitting. This causes a resonant absorption of the microwave which is accompanied by a slight increase in the signal reflected from the cavity. Contrary to optical or transport measurements, electron spin resonance is probed by varying the $\mathbf{B}_0$ external field and keeping the excitation frequency stable. This stems from the technical difficulty of producing stable broadband microwave equipment.

The identification of the minuscule ESR signal from the noisy detector signal requires a technique called phase sensitive or lock-in detection. This scheme allows the weak response of a probed phenomenon to be distinguished from the noisy environment by modulating a weak signal at a high frequency and detecting at the same frequency. In ESR spectrometers the linear sweep external $\mathbf{B}_0$ magnetic field is modulated by the built-in “modulation coils” of the cavity. It operates with the amplified AC reference signal of the lock-in detector and produces a $\mathbf{B}_{\text{mod}}(f_{\text{mod}}) \parallel \mathbf{B}_0$ field and alternates at high frequencies.

The effect of the modulation can be calculated from the detector output induced by the response of the cavity at resonance. The power emitted by the cavity at resonant absorption is given by the following formula [24]:

---

[1] The cavity resonance should not be mistaken for the resonant absorption due to the electron spin flip.

$$P = \frac{1}{\pi \mu_0} \left| \mathbf{B}_1 \right|^2 \omega \chi''(\omega) V \tag{4.2}$$

where μ_0 is the vacuum permeability, $\mathbf{B}_1$ is the alternating excitation field of the cavity.

The detector voltage difference at resonant absorption is proportional to the macroscopic magnetic moment of the studied sample [46, 48]:

$$\Delta U_{\text{det}} \propto \mathbf{m} \propto \chi'' V B_1 \tag{4.3}$$

By taking the series expansion of χ'' and neglecting higher order terms, the lock-in scheme averages out the constant term and preserve the first derivative of the susceptibility:

$$\chi'' \approx \chi''\big|_{B_0} + \left.\frac{d\chi''}{dB}\right|_{B_0} \Delta B. \tag{4.4}$$

As a result, the output of the lock-in amplifier will be proportonal to the following quantities:

$$U_{\text{Lock-in}} \propto \frac{d\chi''}{dB_0} V B_1 B_{\text{mod}} \propto \frac{d\chi''}{dB_0} V \sqrt{P_{\text{MW}}} B_{\text{mod}}, \tag{4.5}$$

where $P_{\text{MW}} \propto \left| \mathbf{B}_1 \right|^2$ was taken into account.

As the magnitude of the processed signal is proportional to $\frac{d\chi''}{dB_0}$, resonances arise as derivative Lorentzian curves in the ESR spectra (as depicted in Fig. 4.5.).

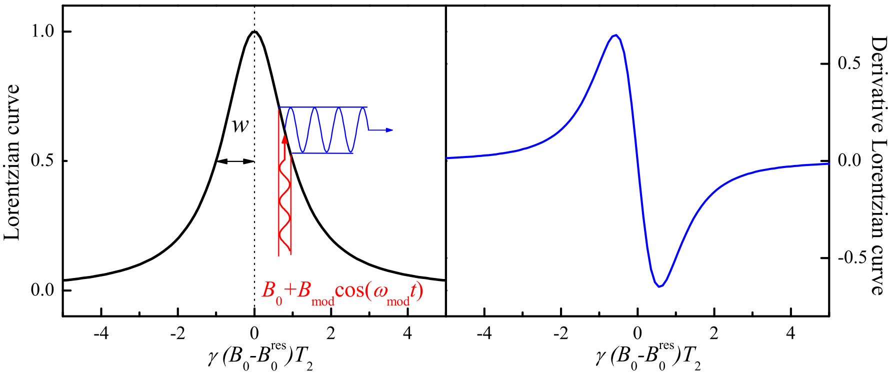

Figure 4.5: *Effect of the lock-in method on the Lorentzian lineshape.*

As opposed to commercial solutions (e.g. Bruker), the modified JEOL setup has a few unique properties, which are highlighted here. The determination of the magnetic field was originally calculated from the current of the electromagnet. To ensure precise scale calibration, a Hall effect sensor was added. The JEOL spectrometer setup was optimized for experiments on high loss, metallic samples, by utilizing a low Q cavity ($Q \approx 1000$).

The extreme high conductance of some samples significantly lowered the quality factor of the cavity and in several instances, critical coupling could not be achieved. The same was true for low conductance samples, as critical coupling was out of the range of iris operation.

In the case of both spectrometers, communication with the instruments and data acquisition is handled by computer software.

Both setups can accommodate temperature dependent experiments. The Bruker system is operated with a commercial liquid helium cryostat, covering the 3.5-250 K range. The temperature is adjusted with built in PID controlled heater. Temperature control in the JEOL system io realized with a home-made nitrogen gas circulation system. Operation is possible up to $\sim$ 700 K and down to a few degrees above the boiling point of liquid nitrogen (77 K).

4.2.2 High frequency ESR

High field measurements were performed on a home built quasi-optical continuous wave ESR spectrometer [49] at 111 GHz ($\sim$ 4 T resonance field) in the laboratory of Prof. András Jánossy.

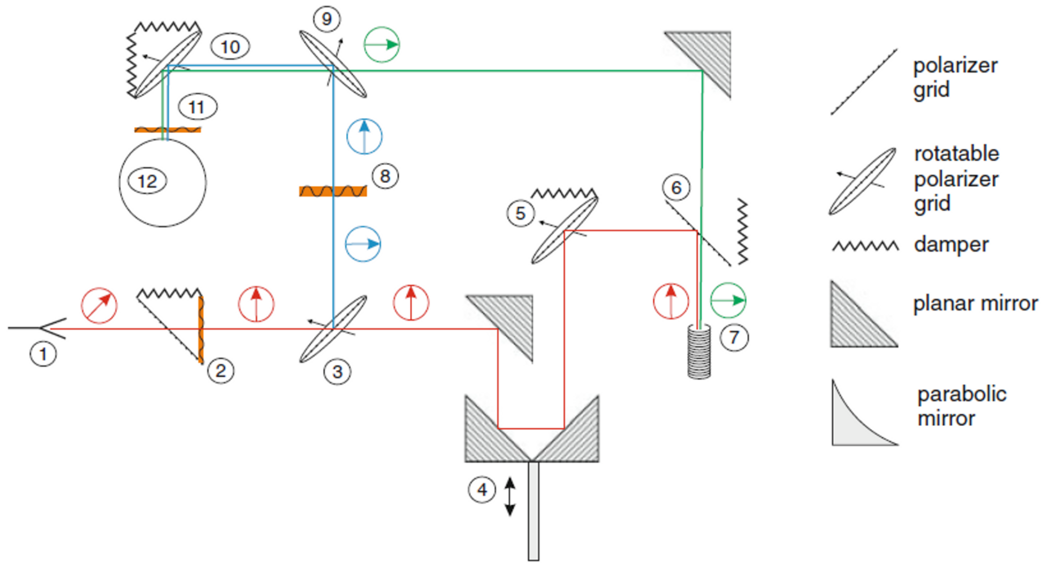

Figure 4.6: *Schematics of the high frequency ESR setup. The microwave radiation is emitted from the (1) microwave source, passes through the (2) isolator (45° Faraday rotator), (3) beam splitter, (4) phase shifter, (5) attenuator and enters the (7) probe head through the (6) grid for "polarization coding". The reference signal is directed towards the (8) 90° Faraday rotator, and then joins the signal with orthogonal polarization at grid (9). Finally the signal and the reference, added at the (10) rotating grid, enter the (12) detector isolated from the bridge by the (11) 45° Faraday rotator (from [49])*

Waveguides and cavity resonators are not applicable for microwaves of such small wavelengths, hence the microwave bridge is replaced by an elaborate system of quasi-optical elements (Fig. 4.6) and more sensitive detectors. The resonance field associated with these higher frequencies requires the use of superconducting magnets. The higher resonance field significantly increases the resolution of the measurements, however this advantage also inhibits most CESR experiments. The skin effect is significantly magnified, penetration depth is 3.5 times smaller for 111 GHz than for the 9 GHz studies. The liquid helium cryostat limited the studied temperature range to below 270 K.

Chapter 5

Results and discussion

The present chapter exhibits the results of my studies, their evaluation and the conclusions. I focus on stage 1 potassium graphite (KC_8), synthesized with different starting graphite materials. The results are discussed in the theoretical framework of electron spin relaxation.

5.1 The CESR signal of doped graphite

The first step in the investigation of CESR in potassium graphite was a preliminary study of the effect of doping in graphite. The effect of the doping time was studied on a graphite powder sample mixed with Mn:MgO. Intercalation was done at 300°C in intervals with an extremely narrowed doping ampoule, to allow sufficient control over the intercalation process. The CESR spectrum was acquired after each step.

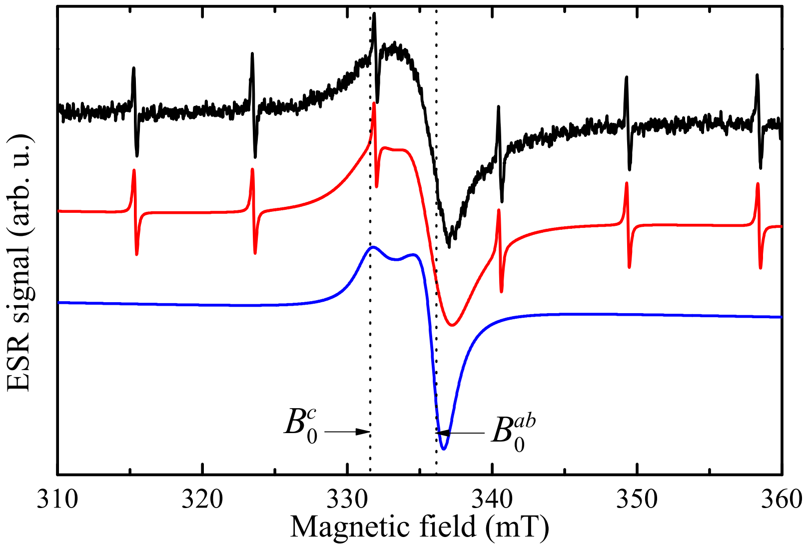

Figure 5.1: *CESR spectrum of pristine graphite powder mixed with Mn:MgO (black curve) and the corresponding powder average fit (red curve), and the powder average simulated for narrower lines (blue curve). The sextet line arises from the hyperfine splitting of the* Mn^{2+} *ions.*

The 2 + 1 dimensional structure of pristine graphite is reflected in its electronic properties. The g-factor and line-width are anisotropic, especially at low temperatures [50, 51]. For a powder sample, the anisotropy is expected to produce a curious shape as the measured signal is a powder average of the g-factor and line-width over the possible orientations of the graphite microcrystallites. As Fig. 5.1 shows, the measured spectra and the simulated powder average fits are in a good agreement.

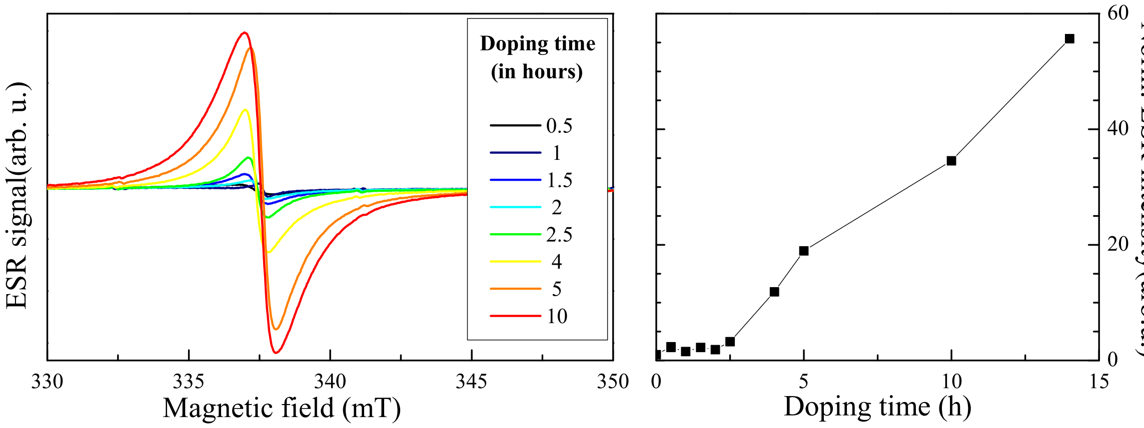

Figure 5.2: *Doping time dependence of the CESR spectrum (left) and CESR intensity (right).*

The doping time dependence of the ESR spectra is presented in Fig. 5.2. A symmetric line emerges beside the anisotropic signal of pristine graphite for low doping. As the doping time increases, the line dominates over the other signal. The onset of the doping is slow, however once it occurs, the signal intensity steadily increases without a significant change in the line-width. The unchanged line-width indicates stable conditions and the formation of the same stage configuration for short and long doping times. The signal intensity did not change after 25 hours of doping which indicated the saturation of the doping. For normal doping vessels this time was considerably shorter.

The doping dependence of the ESR signals was followed by the investigation of saturation doped compounds from both HOPG and graphite powder hosts prepared as described in Sec. 4.1. The X-band spectra of the stage I potassium doped graphite compounds are shown in Fig. 5.3. Dysonian line shapes [32, 33] are observed, characteristic of conducting samples, where only the surface conduction electrons within the skin depth are affected by the microwave excitation. As we move from the HOPG slab to the well dispersed powder the asymmetry is less profound and is accompanied by stronger signals. This is due to the decrease in the ratio of the grain size and skin depth, which results in a better microwave penetration for separated crystallites. In all cases, asymmetry is moderate enough to fit the spectra with a combination of absorption and dispersion Lorentzian lines [35]. Intensity, resonance field, and line-width are acquired from these.

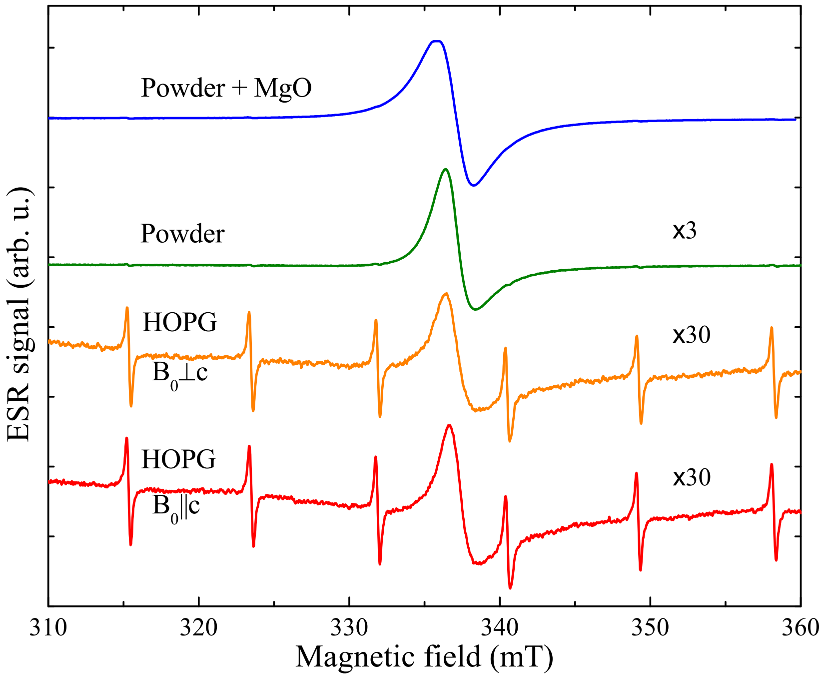

Figure 5.3: *X-band CESR spectra of* KC_8*. The sextet line stems from the* Mn^{2+} *g-factor reference. Note the asymmetric line shape that is characteristic for conductive samples.*

5.2 CESR measurement of spin susceptibility and density of states

The mixed powder offers the opportunity to determine the Fermi level density of states for KC_8 through spin resonance measurements [52].

In Sec. 3.1.2 it was shown that the resonance is characterized by a Lorentzian curve and Eq. (3.17) showed that I its intensity is governed by the total static susceptibility ($\chi_0 V$) of the sample. Sec. 4.2.1 showed that the measured signal also depends on the instrumental parameters of the setup: the P microwave power and the B_{mod} modulation field.

$$I \propto \chi_0 V \sqrt{P} B_{\text{mod}} \tag{5.1}$$

The χ_0 static susceptibility is either a χ_0^{Curie} Curie susceptibility or a χ_0^{Pauli} Pauli susceptibility, if the resonance stems from localized spins or a delocalized electron gas, respectively. The susceptibilities were introduced in Sec. 3.2 as

$$\chi_0^{\text{Curie}} V = \frac{S(S+1)}{3k_{\text{B}}T} g_e^2 \mu_0 \mu_{\text{B}}^2 N_{\text{ion}}, \quad \text{and} \tag{5.2}$$

$$\chi_0^{\text{Pauli}} V = \frac{1}{4} g_e^2 \mu_0 \mu_B^2 g(\varepsilon_{\text{F}}), \tag{5.3}$$

where N_{ion} is the number of ions, in the case of Mn:MgO, it is equal to the number of unit cells ($N_C = N_{Spin}$)

For Mn^{2+} ions, a spin of $S_{\mathrm{Mn}^{2+}} = \frac{5}{2}$ yields $S(S+1)_{\mathrm{Mn}^{2+}} = \frac{35}{4}$, however only the $\left|-\frac{1}{2}\right\rangle \Leftrightarrow \left|\frac{1}{2}\right\rangle$ transitions of these ions are detectable in ESR. This means that $S(S+1)$ is replaced by an effective value of $\langle S(S+1)\rangle_{\mathrm{Mn}^{2+}} = \frac{9}{4}$, which is derived from the matrix element of mentioned spin flip transition.

The $c_{\mathrm{Mn}^{2+}} = 1.5$ ppm concentration of Mn^{2+} ions in MgO was determined through signal intensity comparison with a known amount of $CuSO_4 \cdot 5H_2O$ with $S_{\mathrm{Cu}^{2+}} = \frac{1}{2}$ and $S(S+1)_{\mathrm{Cu}^{2+}} = \frac{3}{4}$. Thus we acquire the molar susceptibility of the Mn:MgO mixture (in CGS units): $\chi_{0,mol}^{\mathrm{Curie}}(\mathrm{Mn{:}MgO}) = 5.641 \cdot 10^{-9} \frac{\mathrm{emu}}{\mathrm{mol}}$.

With this susceptibility reference, the ratio of the intensities yields the susceptibility of the sample:

$$\frac{I_{\mathrm{Sample}}}{I_{\mathrm{Mn:MgO}}} = \frac{\chi_{0,\mathrm{mol}}\big(\mathrm{Sample}\big)}{\chi_{0,\mathrm{mol}}\big(\mathrm{Mn{:}MgO}\big)} \frac{n_{\mathrm{Sample}}}{n_{\mathrm{Mn:MgO}}} \tag{5.4}$$

$$\chi_{0,\mathrm{mol}}\big(\mathrm{Sample}\big) = \chi_{0,\mathrm{mol}}\big(\mathrm{Mn{:}MgO}\big) \frac{I_{\mathrm{Sample}}}{I_{\mathrm{Mn:MgO}}} \frac{n_{\mathrm{Mn:MgO}}}{n_{\mathrm{Sample}}} \tag{5.5}$$

Similarly, the density of states of a Pauli susceptibility sample is given by the ratio of intensities with a reference

$$\frac{I_{\mathrm{Pauli}}}{I_{\mathrm{Curie}}} = \frac{1}{S(S+1)} \frac{3}{4} k_B T g(\varepsilon_{\mathrm{F}}) \frac{N_{\mathrm{Pauli}}}{N_{\mathrm{Curie}}} \tag{5.6}$$

$$g(\varepsilon_{\mathrm{F}}) = \frac{I_{\mathrm{Pauli}}}{I_{\mathrm{Curie}}} S(S+1) \frac{4}{3} N_{\mathrm{ion}} \frac{1}{k_{\mathrm{B}} T} \tag{5.7}$$

where $g(E_{\mathrm{F}})$ is the density of states at the Fermi level, measured in units $\frac{\mathrm{states}}{\mathrm{eV \cdot C\ atom}}$.

These susceptibility measurements require high reproducibility, this demands the use of the same instrumental parameters and place the sample in the same position every time. Through mixing with an equal mass of Mn:MgO two problems due to the skin effect were circumvented. Firstly, the separation of the graphite crystals increased microwave penetration and thus the S/N ratio. Secondly, the reduction of the studied volume does not impede the calculation of the density of states as only the relative intensities are required for the homogeneous powder. A modulation field of $B_{\mathrm{mod}} = 10^{-4}$ mT enhance the signal, but did not lead to a distorted resonance line. Microwave power was set to $P = 10$ mW as Mn^{2+} lines were not distinguishable at lower powers. This is undesirable as it leads to microwave saturation for the manganese. Thus such measurements, where the reference manganese signal is reduced due to saturation, produce lower intensities than expected and seemingly increase the susceptibility and density of states values. Despite this, it is still applicable with an error well within an order of magnitude.

Table 5.1 gathers density of states and spin susceptibility measurements. The data are in agreement with values from literature [53–55].

Table 5.1: *Density of states and spin susceptibilities in* KC_8.

	χ_0 (10^{-6} emu/g)	$g(E_F)$ (states/eV·C atom)
CESR	0.92(3)-0.95(6)	0.33(5)-0.34(7)
specific heat [53, 54]	-	0.327,0.35
susceptibility measurement [55]	0.62	-

5.3 Testing the Elliott-Yafet mechanism in KC_8

The validity of Elliott-Yafet theory is tested in KC_8 measurement of the shift in the g-factor and comparison of the temperature dependence of the line-width with resistivity data from literature.

CESR spectra of both HOPG and powder morphologies were acquired for the temperature range of 4-500 K with a typical microwave power of 10 mW and modulation of 0.1-0.2 mT. The high conductance of the samples significantly lowered the quality factor of the cavity and in several instances critical cavity coupling could not be achieved. HOPG samples are measured for both c-axis and in-plane (ab) B_0 external fields, the orientation of the fields and the sample are shown in Fig. 5.4.

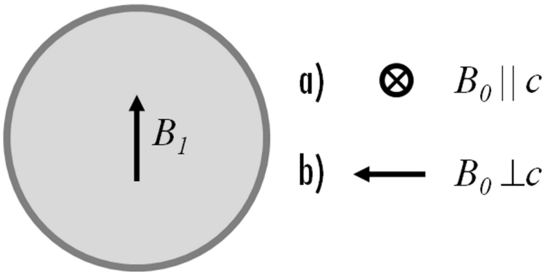

Figure 5.4: *Orientation of* B_0 *and* B_1 *with regard to the disk shaped HOPG sample.*

Fig. 5.5. shows the temperature dependence of the ESR line-width—proportional to the inverse spin relaxation time ($\Delta B = \frac{1}{\gamma T_2}$)—for different compounds. Doped HOPG samples were only studied up to 450 K, above this temperature the potassium on the surface of the graphite slab begins to evaporate and simultaneously diffuse into the inside of the disk, effectively dedoping the sample surface (which is otherwise sensed by ESR). The helium cryostat of the high field spectrometer limits the studied temperature range of such measurements to below 270 K.

The HOPG and powder samples show the same trends in line-width temperature dependence for both frequencies. The curves differ mainly in a constant line-width term and only slightly in the line-width term from homogeneous broadening. The data for the HOPG sample are in agreement with data obtained by Lauginie *et al.* in [56] with

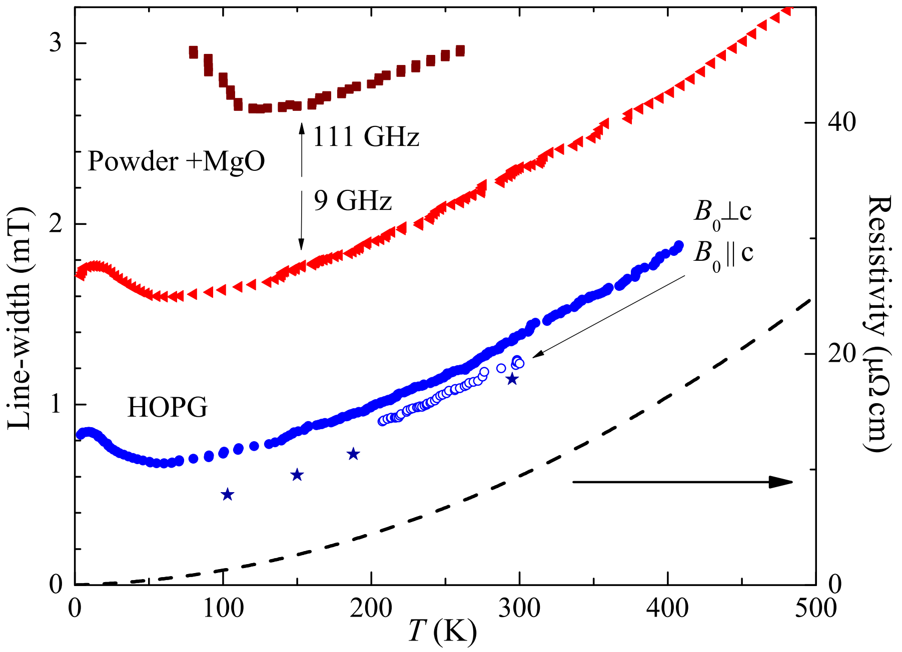

Figure 5.5: *Temperature dependence of the CESR line-width in* KC_8 *(left axis):* $B_0 \perp c$ *(●) and* $B_0 \| c$ *(○) orientated HOPG, and separated powder (◀) at 9 GHz, and at 111 GHz (■). X-band data on HOPG with* $B_0 \| c$ *(★) from Ref. [56]. is shown for comparison. Note the slight asymmetry of HOPG orientations and the larger line-width for the 111 GHz measurement. Dashed black curve shows in-plane resistivity data (right axis) from Ref. [57].*

a minimal anisotropy for the two geometries. Opposed to the linear temperature dependence shown in [56], we encounter a quadratic term in agreement with in-plane resistivity measurements [57, 58]. These references give an empirical temperature dependence of $A + BT + CT^2$, where the constant term is the residual resistivity, the electron-phonon coupling is responsible for the linear term and the T^2 term arises due to electron-electron interaction. Such quadratic fits of $\Delta B(T)$ with an independent A constant term and a fixed ratio of B/C corresponding to resistivity data from [57] allowed the separation of the homogeneous broadening coming from spin relaxation and to identify the proportionality of T_1 and τ. This is elaborated later in the discussion.

Residual line-widths of $\Delta B_0^{\mathrm{HOPG}} = 0.5$-$0.6$ mT and $\Delta B_0^{\mathrm{powder}} = 1.7$ mT were found at 9 GHz for the HOPG and separated powder samples, respectively. The difference in the residual relaxation term can be attributed to the higher disorder in well-separated powder, e.g.: due to grain boundaries, surface effects, impurities. High field measurements at 111 GHz ($\sim$ 4 T field) were performed to identify the g-factor anisotropy induced frequency dependent contributions to the line-width [59]. X-band and high field spectra show an average line-width difference of 0.72 mT, which yields a negligible contribution of $\Delta B_{\mathrm{anis}} \approx 0.06$ mT at 9 GHz stemming from anisotropy.

Fig. 5.6 indicates that the intensity of the CESR signal decreases with decreasing T. As the conductivity increases and the penetration depth decreases, the studied volume of the sample is reduced, resulting in a smaller signal intensity.

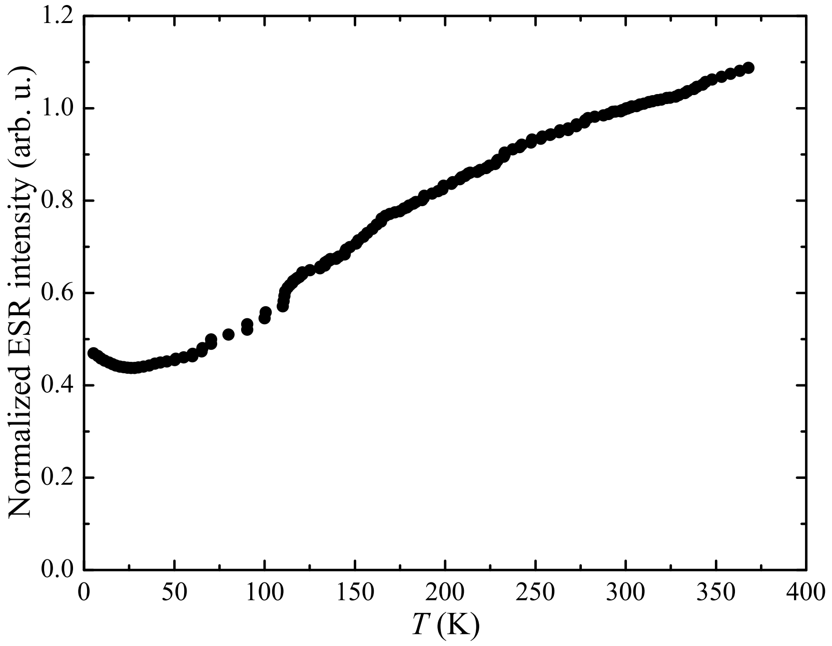

Figure 5.6: *Temperature dependence of the ESR signal intensity for a KC_8 sample prepared from HOPG.*

The increase in the line-width at low temperatures ($T < 50$ K) can be attributed to localized paramagnetic impurities. In the so-called bottleneck regime [60] the impurities and the conduction electrons have a common resonance and the line-width will be a combination of the two relaxation rates, weighted by their susceptibilities. Thus at low temperatures the impurities are dominant due to the nature of the Curie susceptibility. This is further proven by the observed low temperature increase in the intensity.

The validity of the Elliott-Yafet theory for monovalent and noble metals was originally shown by Beuneu and Monod [39, 40]. Their works identified the connection between the ratio of the phonon contribution for the line-width and resistivity to the g-factor shift, as predicted by the theory. In the following, I follow the validating procedure introduced by Beuneu and Monod to identify whether the Elliott-Yafet behavior is observed in KC_8.

As previously shown, spin relaxation rates and resistivity of KC_8 exhibit the same temperature dependence and their homogeneous terms are proportional, as predicted by the Elliott-Yafet theory. However, this proportionality has to be in accordance with $(\Delta g)^2$.

Room temperature g-factors are acquired by comparison to a manganese reference ($g_{\mathrm{Mn}^{2+}} = 2.0014$) [61] where second order hyperfine interaction was taken into account. Results are summarized in Table 5.2 along with data from previous studies [56], error bars are calculated from the variance of the data for different samples. While measurements produced values with the same difference as in the literature, their values are lower by 0.0003 in both orientations. This result is further confirmed by powder measurements where g-factors close to g_0 are in agreement with powder averages from HOPG data. The higher values in the data probably are a result of empirical analysis of the Dysonian lines, as before computer assisted data evaluation was available, the Dysonian resonance field was acquired from the intersection of the resonance curve and baseline. This value is systematically higher than the true resonance field, which can be acquired from curve fitting.

Table 5.2: *g-factor data and its shift with respect to g_e for the different KC$_8$ samples.*

Host compound	Orientation	g	$\Delta g \times 10^{-4}$
HOPG (Ref. [56].)	$B_0 \parallel c$	2.0016	-7
HOPG (Ref. [56].)	$B_0 \perp c$	2.0030	7
HOPG (measured)	$B_0 \parallel c$	2.0027	4.03 ± 0.61
HOPG (measured)	$B_0 \perp c$	2.0013	-9.84 ± 0.95
HOPG (corrected)	$B_0 \parallel c$	2.0033	10.31 ± 0.61
HOPG (corrected)	$B_0 \perp c$	2.0036	13.03 ± 0.95
powder		2.0024	1.54 ± 0.51
powder+MgO		2.0024	0.99 ± 0.52

To identify the intrinsic g-shift of the material the coupling of the electrons to the macroscopic magnetic susceptibility [60] was taken into account:

$$g_{\text{meas}} = g_{\text{intr}} \left(1 + \lambda \chi^0\right) = g_{\text{intr}} + \Delta g(\chi^0) \tag{5.8}$$

where $\Delta g(\chi^0)$ is the macroscopic magnetic susceptibility dependent g-shift and λ is the coupling coefficient.

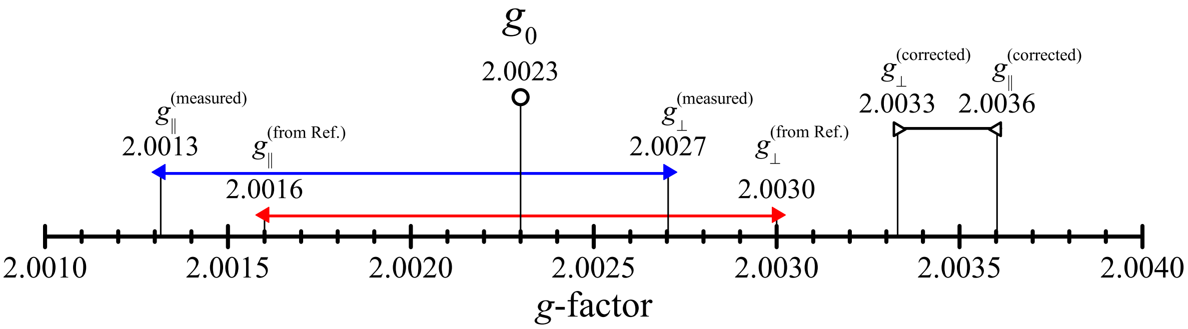

Figure 5.7: *Illustration of g-factors for KC$_8$: the g_0 = 2.0023 free electron g-factor (◯), data from Ref. [56] (◀ and ▶), current measurements (◀ and ▶), and current measurements corrected by coupling to macroscopic susceptibility (◁ and ▷).*

The strength and sign of the coupling for graphite is derived from the diamagnetic χ_c^{graphite} susceptibilities [55] and positive Δg values [62]. Assuming that λ does not vary between graphite and KC$_8$, the KC$_8$ macroscopic susceptibilities [55] yield $\Delta g_{\perp} = -0.000628$ and $\Delta g_{\parallel} = -0.00229$. Using these values, intrinsic g-factors are obtained for both orientations independently (see Table 5.2.). The corrected Δg values both bare positive signs and a much lower anisotropy than the non-corrected values. The significant points for the HOPG sample are depicted in Fig. 5.7.

The slight anisotropy of both the derived intrinsic g-shifts and the HOPG line-widths for the $B_0 \perp c$ and $B_0 \parallel c$ setups contradicts simple theoretical 2D models, which predict no shift of the g-factor for an in-plane field and no relaxation for a perpendicular external magnetic field. However the lack of extreme anisotropy is not specific to the model system, as it was observed in graphene spin transport measurements [63] as well. Furthermore, the magnitude and sign of 10-15 % line-width anisotropy is in agreement with $\sim$ 20 % values observed by Tombros *et al.* in [63]. This supports the assumption that a weakly anisotropic Elliott-Yafet mechanism is responsible for the spin relaxation[1].

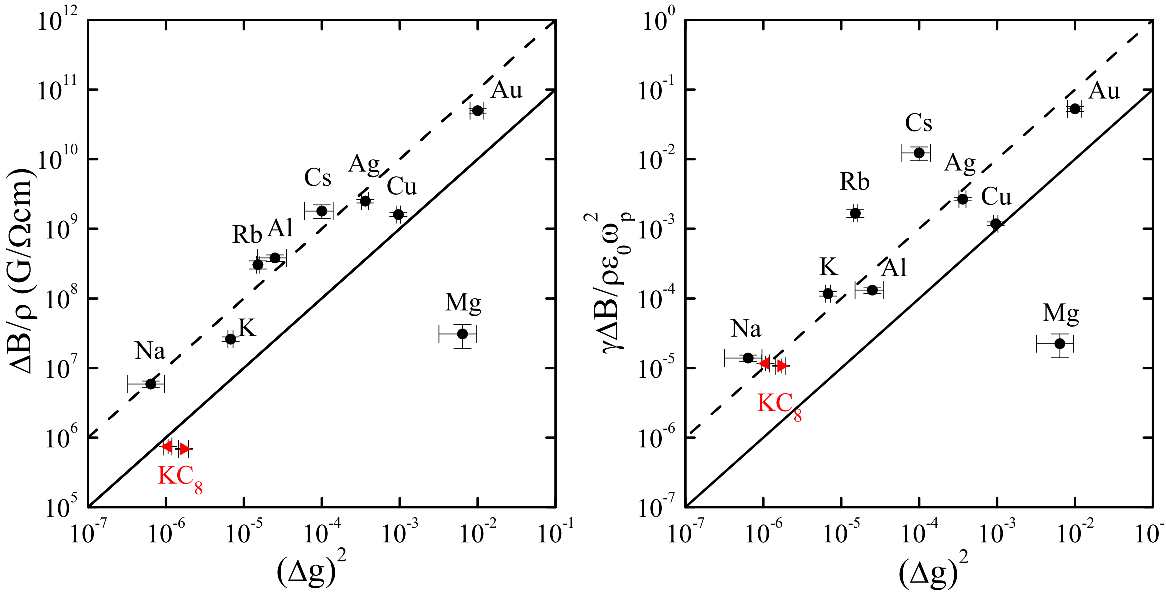

Figure 5.8: *Original (left) and corrected (right) Beuneu-Monod plot showing the ratio of the line-width and resistivity* ($\frac{\Delta B}{\rho}$, *left plot) and the dimensionless reduced line-width* ($\gamma\Delta B/\rho\varepsilon_0\omega_p^2$, *right plot) as a function of* $(\Delta g)^2$ *and for pure metals [39](○) and the KC$_8$ compound for* $\perp$ *(◀) and* $\parallel$ *(▶).*

In the original study of pure metals, the $\frac{\Delta B}{\rho}$ ratio was found to be linearly proportional to $(\Delta g)^2$ with a constant coefficient of $10^{11}\frac{\mathrm{G}}{\Omega\mathrm{cm}}$, neglecting the variation of ω_p^2 from metal to metal. To properly compare other data for KC$_8$, plasma frequencies [64, 65] are taken into account:

$$\frac{\Delta B}{\rho} = \frac{ne^2}{\gamma m^*}\frac{\tau}{T_1} = \frac{\varepsilon_0\omega_\mathrm{p}^2}{\gamma}\frac{\tau}{T_1} = \frac{\varepsilon_0\omega_\mathrm{p}^2}{\gamma}\frac{\alpha_1}{\alpha_2^2}(\Delta g)^2 \tag{5.9}$$

With the variation of $\alpha_{1,2} = 1..10$ from material to material, points in the log-log plot should fall within the solid and dashed lines corresponding to the cases of $\frac{\tau}{T_1} = 10(\Delta g)^2$ and $\frac{\tau}{T_1} = (\Delta g)^2$, respectively.

---

[1] As the Elliott-Yafet theory was formulated for metals it is based on an isotropic model.

This correction yields KC_8 values that fit well with $\frac{\tau}{T_1} = 10(\Delta g)^2$ curve, in agreement with the findings on metals. However, the correction weakens the agreement for most alkali metals (Na, Rb, Cs). It is beyond the scope of these experiments to explain this curious result.

Chapter 6

Summary

In my thesis, I presented an epitome of my research project involving sample synthesis, characterization measurements, and data evaluation.

It consists of a summary of the literature relevant for the materials of interest, an introduction to magnetic resonance and the specifics of conduction electron resonance, details of instrumentation and sample preparation, and my results with conclusions.

I described the setup of the two zone vapor method synthesis which was implemented as a part of my project. I gave details on the temperature setup needed to achieve various stages for different intercalants.

The presented measurements were aimed at the stage I compound of potassium with different grapite morphologies. The technique of choice to characterize the material properties, which are relevant for spintronics, was CESR. First, I demonstrated the applicability of CESR for DOS and spin susceptibility measurements. The main point of my work was to test spin relaxation in KC_8.

I found the Elliott-Yafet theory to be valid for KC_8 compounds, with the proportionality of the homogeneous line width and in-plane resistivity in agreement with the g-factor shift as for metals. Band calculations, ARPES measurements, and the similarly weak anisotropy observed for graphene suggest that the spin relaxation of graphene is governed by the same mechanism.

My work on this project during my BSc [52] and MSc produced one published [66] and one submitted paper [67]. A third manuscript has been prepared from the results of this thesis and awaits submission to a peer-reviewed scientific journal [68].

Although not part of this thesis, I participated in the development of a modern Raman spectrometer at the University of Vienna. The result was published in the Review of Scientific Instruments [69]. It also produced a poster presentation at IWEPNM 2011, Kirchberg and a submitted conference proceedings [70].

References

[1] G. E. Moore, “Cramming More Components onto Integrated Circuits,” *Electronics*, vol. 38, pp. 114–117, Apr. 1965.

[2] P. L. McEuen, “Nanotechnology - Carbon-based electronics,” *Nature*, vol. 393, pp. 15–17, May 1998.

[3] K. S. Novoselov, A. K. Geim, S. V. Morozov, D. Jiang, Y. Zhang, S. V. Dubonos, I. V. Grigorieva, and A. A. Firsov, “Electric field effect in atomically thin carbon films,” *Science*, vol. 306, pp. 666–669, 2004.

[4] I. Žutić, J. Fabian, and S. D. Sarma, “Spintronics: Fundamentals and applications,” *Rev. Mod. Phys.*, vol. 76, pp. 323–410, 2004.

[5] N. Tombros, C. Jozsa, M. Popinciuc, H. T. Jonkman, and B. J. van Wees, “Electronic spin transport and spin precession in single graphene layers at room temperature,” *Nature*, vol. 448, pp. 571–574, Aug 2007.

[6] S. Cho, Y.-F. Chen, and M. S. Fuhrer, “Gate-tunable graphene spin valve,” *Applied Physics Letters*, vol. 91, no. 12, p. 123105, 2007.

[7] M. S. Dresselhaus and G. Dresselhaus, “Intercalation compounds of graphite,” *Advances in Physics*, vol. 51, pp. 1–186, Jan 2002.

[8] A. Grüneis, C. Attaccalite, A. Rubio, D. V. Vyalikh, S. L. Molodtsov, J. Fink, R. Follath, W. Eberhardt, B. Büchner, and T. Pichler, “Electronic structure and electron-phonon coupling of doped graphene layers in kc_8,” *Phys. Rev. B*, vol. 79, p. 205106, May 2009.

[9] B. Dóra, F. Murányi, and F. Simon, “Electron spin dynamics and electron spin resonance in graphene,” *EPL*, vol. 92, p. 17002, 2010.

[10] N. D. Mermin and H. Wagner, “Absence of ferromagnetism or antiferromagnetism in one- or two-dimensional isotropic heisenberg models,” *Phys. Rev. Lett.*, vol. 17, pp. 1133–1136, Nov 1966.

[11] Y. Zhang, Y.-W. Tan, H. L. Stormer, and P. Kim, “Effect of ^{13}C isotopic substitution on the Raman spectrum of C_{60},” *Nature*, vol. 438, p. 201, 2005.

[12] K. S. Novoselov, A. K. Geim, S. V. Morozov, D. Jiang, M. I. Katsnelson, I. V. Grigorieva, S. V. Dubonos, and A. A. Firsov, “Two-dimensional gas of massless Dirac fermions in graphene,” *Nature*, vol. 438, pp. 197–200, 2005.

[13] K. S. Novoselov, Z. Jiang, Y. Zhang, S. V. Morozov, H. L. Stormer, U. Zeitler, J. C. Maan, G. S. Boebinger, P. Kim, and A. K. Geim, “Room-temperature quantum hall effect in graphene,” *Science*, vol. 315, no. 5817, p. 1379, 2007.

[14] A. H. Castro Neto, F. Guinea, N. M. R. Peres, K. S. Novoselov, and A. K. Geim, “The electronic properties of graphene,” *Rev. Mod. Phys.*, vol. 81, pp. 109–162, Jan 2009.

[15] P. R. Wallace, “The Band Theory of Graphite,” *Physical Review*, vol. 71, pp. 622–634, May 1947.

[16] S. Reich, J. Maultzsch, C. Thomsen, and P. Ordejón, “Tight-binding description of graphene,” *Phys. Rev. B*, vol. 66, p. 035412, Jul 2002.

[17] A. Grüneis, C. Attaccalite, L. Wirtz, H. Shiozawa, R. Saito, T. Pichler, and A. Rubio, “Tight-binding description of the quasiparticle dispersion of graphite and few-layer graphene,” *Phys. Rev. B*, vol. 78, p. 205425, Nov 2008.

[18] R. Saito, G. Dresselhaus, and M. Dresselhaus, *Physical Properties of Carbon Nanotubes.* Imperial College Press, 1998.

[19] A. Grüneis, C. Attaccalite, T. Pichler, V. Zabolotnyy, H. Shiozawa, S. L. Molodtsov, D. Inosov, A. Koitzsch, M. Knupfer, J. Schiessling, R. Follath, R. Weber, P. Rudolf, L. Wirtz, and A. Rubio, “Electron-electron correlation in graphite: A combined angle-resolved photoemission and first-principles study,” *Phys. Rev. Lett.*, vol. 100, p. 037601, Jan 2008.

[20] H. Schomerus, “Helical scattering and valleytronics in bilayer graphene,” *Phys. Rev. B*, vol. 82, p. 165409, Oct 2010.

[21] N. B. Hannay, T. H. Geballe, B. T. Matthias, K. Andres, P. Schmidt, and D. MacNair, “Superconductivity in graphitic compounds,” *Phys. Rev. Lett.*, vol. 14, pp. 225–226, Feb 1965.

[22] Z.-H. Pan, J. Camacho, M. H. Upton, A. V. Fedorov, C. A. Howard, M. Ellerby, and T. Valla, “Electronic Structure of Superconducting KC_8 and Nonsuperconducting LiC_6 Graphite Intercalation Compounds: Evidence for a Graphene-Sheet-Driven Superconducting State,” *Phys. Rev. Lett.*, vol. 106, p. 187002, May 2011.

[23] Y. K. Zavoisky, *Paramagnetic Absorption in Perpendicular and Parallel Fields for Salts, Solutions and Metals.* PhD thesis, Kazan State University, 1944.

[24] C. P. Slichter, *Principles of Magnetic Resonance.* New York: Spinger-Verlag, 3rd ed. 1996 ed., 1989.

[25] W. Gerlach and O. Stern, “Das magnetische Moment des Silberatoms,” *Zeitschrift fur Physik*, vol. 9, pp. 353–355, Dec. 1922.

[26] P. A. M. Dirac, “The quantum theory of the electron,” *Proceedings of the Royal Society of London. Series A*, vol. 117, no. 778, pp. 610–624, 1928.

[27] F. Bloch, “Nuclear induction,” *Phys. Rev.*, vol. 70, pp. 460–474, Oct 1946.

[28] N. W. Ashcroft and N. D. Mermin, *Solid State Physics.* Philadelphia: Saunders College Publishing, 1976.

[29] G. R. Eaton, S. S. Eaton, and K. M. Salikhov, eds., *Foundations of Modern EPR.* Singapore: World Scientific, 1998.

[30] Y. Yafet, “Calculation of the g factor of metallic sodium,” *Phys. Rev.*, vol. 85, p. 478, Feb 1952.

[31] T. W. Griswold, A. F. Kip, and C. Kittel, “Microwave spin resonance absorption by conduction electrons in metallic sodium,” *Phys. Rev.*, vol. 88, pp. 951–952, Nov 1952.

[32] G. Feher and A. F. Kip, “Electron Spin Resonance Absorption in Metals. I. Experimental,” *Physical Review*, vol. 98, p. 337, 1955.

[33] F. J. Dyson, “Electron Spin Resonance Absorption in Metals. II. Theory of Electron Diffusion and the Skin Effect,” *Physical Review*, vol. 98, p. 349, 1955.

[34] R. J. Elliott, “Theory of the Effect of Spin-Orbit Coupling on Magnetic Resonance in Some Semiconductors,” *Phys. Rev.*, vol. 96, pp. 266–279, Oct 1954.

[35] L. Walmsley, “Translating conduction-electron spin-resonance lines into lorentzian lines,” *Journal of Magnetic Resonance, Series A*, vol. 122, no. 2, pp. 209 – 213, 1996.

[36] Y. Yafet, “g factors and spin-lattice relaxation of conduction electrons,” in *Advances in Research and Applications* (F. Seitz and D. Turnbull, eds.), vol. 14 of *Solid State Physics*, pp. 1 – 98, Academic Press, 1963.

[37] J. Fabian and S. D. Sarma, “Spin relaxation of conduction electrons,” *J. Vac. Sci. Technol. B*, vol. 17, no. 4, pp. 1708–1715, 1999.

[38] M. G. Munzenberg, “Magnetization dynamics: Ferromagnets stirred up,” *Nature Materials*, vol. 9, pp. 184–185, 2010.

[39] F. Beuneu and P. Monod, “The elliott relation in pure metals,” *Phys. Rev. B*,

vol. 18, pp. 2422–2425, Sep 1978.

[40] P. Monod and F. Beuneu, "Conduction-electron spin flip by phonons in metals: Analysis of experimental data," *Phys. Rev. B*, vol. 19, pp. 911–916, Jan 1979.

[41] L. Forró and F. Beuneu, "ESR study of weakly irradiated organic conductors: TMTSF-DMTCNQ and (TMTSF)2PF6," *Solid State Communications*, vol. 44, no. 5, pp. 623 – 626, 1982.

[42] J. Fabian and S. Das Sarma, "Spin relaxation of conduction electrons in polyvalent metals: Theory and a realistic calculation," *Phys. Rev. Lett.*, vol. 81, pp. 5624–5627, Dec 1998.

[43] J. Fabian and S. Das Sarma, "Phonon-induced spin relaxation of conduction electrons in aluminum," *Phys. Rev. Lett.*, vol. 83, pp. 1211–1214, Aug 1999.

[44] F. Simon, B. Dóra, F. Murányi, A. Jánossy, S. Garaj, L. Forró, S. Bud'ko, C. Petrovic, and P. C. Canfield, "Generalized Elliott-Yafet Theory of Electron Spin Relaxation in Metals: Origin of the Anomalous Electron Spin Lifetime in MgB_2," *Phys. Rev. Lett.*, vol. 101, p. 177003, Oct 2008.

[45] B. Dóra and F. Simon, "Electron-spin dynamics in strongly correlated metals," *Phys. Rev. Lett.*, vol. 102, p. 137001, Apr 2009.

[46] T. Sándor, "Electron spin resonance study of the N@C60 encapsulated inside single-walled carbon nanotubes," Master's thesis, BME, 2008.

[47] "Bruker BioSpin Corporation `http://www.bruker-biospin.com/cwpractice.html`."

[48] C. P. Poole, *Electron Spin Resonance.* New York: John Wiley & Sons, 1983 ed., 1983.

[49] K. Nagy, D. Quintavalle, T. Fehér, and A. Jánossy, "Multipurpose high-frequency esr spectrometer for condensed matter research," *Applied Magnetic Resonance*, vol. 40, pp. 47–63, 2011.

[50] M. S. Sercheli, Y. Kopelevich, R. R. da Silva, J. H. S. Torres, and C. Rettori, "Evidence for internal field in graphite: a conduction electron spin-resonance study," *Solid State Communications*, vol. 121, no. 9-10, pp. 579 – 583, 2002.

[51] D. L. Huber, R. R. Urbano, M. S. Sercheli, and C. Rettori, "Fluctuating field model for conduction electron spin resonance in graphite," *Phys. Rev. B*, vol. 70, p. 125417, Sep 2004.

[52] G. Fábián, "Electron Spin Resonance in Carbon Nanotubes," Bachelor's Thesis, BME, June 2009.

[53] U. Mizutani, T. Kondow, and T. B. Massalski, "Low-temperature specific heats of graphite intercalation compounds with potassium and cesium," *Phys. Rev. B*, vol. 17, pp. 3165–3173, Apr 1978.

[54] M. G. Alexander, D. P. Goshorn, and D. G. Onn, "Low-temperature specific heat of the graphite intercalation compounds kc_8, csc_8, rbc_8, and their parent highly oriented pyrolytic graphite," *Phys. Rev. B*, vol. 22, pp. 4535–4542, Nov 1980.

[55] F. J. DiSalvo, S. A. Safran, R. C. Haddon, J. V. Waszczak, and J. E. Fischer, "Large anisotropy and stage dependence of the magnetic susceptibility of alkali-graphite intercalation compounds," *Phys. Rev. B*, vol. 20, pp. 4883–4888, Dec 1979.

[56] P. Lauginie, H. Estrade, J. Conard, D. Guérard, P. Lagrange, and M. E. Makrini, "Graphite lamellar compounds epr studies," *Physica B*, vol. 99, no. 1-4, pp. 514 – 520, 1980.

[57] M. Potter, W. Johnson, and J. Fischer, "Transport properties of alkali metal-graphite intercalation compounds," *Solid State Communications*, vol. 37, no. 9, pp. 713 – 718, 1981.

[58] H. Suematsu, K. Higuchi, and S. Tanuma, "Electronic properties of graphite-potassium intercalation compounds. ii. resistivity, hall effect and magnetoresistance," *Journal of the Physical Society of Japan*, vol. 48, no. 5, pp. 1541–1549, 1980.

[59] A. Jánossy, N. M. Nemes, T. Fehér, G. Oszlányi, G. Baumgartner, and L. Forró, "Antiferromagnetic Resonance in the Linear Chain Conducting Polymers RbC_{60} and CsC_{60} ," *Phys. Rev. Lett.*, vol. 79, pp. 2718 – 2721, 1997.

[60] S. E. Barnes, "Theory of electron spin resonance of magnetic ions in metals," *Adv. Phys.*, vol. 30, pp. 801–938, 1981.

[61] A. Abragam and B. Bleaney, *Electron Paramagnetic Resonance of Transition Ions.* Oxford, England: Oxford University Press, 1970.

[62] G. Wagoner, "Spin resonance of charge carriers in graphite," *Phys. Rev.*, vol. 118, pp. 647–653, May 1960.

[63] N. Tombros, S. Tanabe, A. Veligura, C. Jozsa, M. Popinciuc, H. T. Jonkman, and B. J. van Wees, "Anisotropic spin relaxation in graphene," *Phys. Rev. Lett.*, vol. 101, p. 046601, Jul 2008.

[64] J. E. Fischer, J. M. Bloch, C. C. Shieh, M. E. Preil, and K. Jelley, “Reflectivity spectra and dielectric function of stage-1 donor intercalation compounds of graphite,” *Phys. Rev. B*, vol. 31, pp. 4773–4783, Apr 1985.

[65] M. Fox, *Optical Properties of Solids.* Oxford, England: Oxford University Press, 2010.

[66] M. Galambos, G. Fábián, F. Simon, L. Ćirić, L. Forró, L. Korecz, A. Rockenbauer, J. Koltai, V. Zólyomi, A. Rusznyák, J. Kürti, N. M. Nemes, B. Dóra, H. Peterlik, R. Pfeiffer, H. Kuzmany, and T. Pichler, “Identifying the electron spin resonance of conduction electrons in alkali doped SWCNTs,” *physica status solidi (b)*, vol. 246, no. 11-12, pp. 2760–2763, 2009.

[67] P. Szirmai, G. Fábián, B. Dóra, J. Koltai, V. Zólyomi, J. Kürti, N. M. Nemes, L. Forró, and F. Simon, “Density of states deduced from ESR measurements on low-dimensional nanostructures; benchmarks to identify the ESR signals of graphene and SWCNTs.” Submitted to Phys. Status Solidi B, May 2011.

[68] G. Fábián, B. Dóra, A. Antal, T. Fehér, J. Koltai, L. Forró, and F. Simon, “Elliott-Yafet spin relaxation in KC_8: a model system of graphene.” To be submitted to Phys. Rev. B, Jun 2011.

[69] G. Fábián, C. Kramberger, A. Friedrich, F. Simon, and T. Pichler, “A broadband and high throughput single-monochromator raman spectrometer: Application for single-wall carbon nanotubes,” *Review of Scientific Instruments*, vol. 82, no. 2, p. 023905, 2011.

[70] G. Fábián, C. Kramberger, A. Friedrich, F. Simon, and T. Pichler, “Adaptation of a commercial Raman spectrometer for multiline and broadband laser operation.” Submitted to Phys. Status Solidi B, May 2011.